

Thermophysical model for realistic surface layers on airless small bodies: applied to study the spin orientation and surface dust properties of (24) Themis from WISE/NEOWISE multi-epoch thermal lightcurves

LIANG-LIANG YU¹ AND WING-HUEN IP^{1,2}

¹State Key Laboratory of Lunar and Planetary Sciences, Macau University of Science and Technology, Macau, China

²Institute of Astronomy, National Central University, Jhongli, Taoyuan City 32001, Taiwan

(Received February 06, 2021; Revised March 22, 2021; Accepted April 01, 2021)

ABSTRACT

This work proposes a thermophysical model for realistic surface layers on airless small bodies (RSTPM), for the use of interpreting their multi-epoch thermal lightcurves (e.g. WISE/NEOWISE). RSTPM considers real orbital cycle, rotation cycle, rough surface, temperature dependent thermal parameters, as well as contributions of sunlight reflection to observations, hence being able to produce precise temperature distribution and thermal emission of airless small bodies regarding the variations in orbital time scales. Details of the physics, mathematics and numerical algorithms of RSTPM are presented. When used to interpret multi-epoch thermal lightcurves by WISE/NEOWISE, RSTPM can give constraints on the spin orientation and surface physical properties, like mean thermal inertia or mean size of dust grains, roughness fraction, albedo and so on via radiometric procedure. As an application example, we apply this model to the main-belt object (24) Themis, the largest object of the Themis family, which is believed to be the source region of many main-belt comets. We find multi-epoch (2010, 2014-2018) observations of Themis by WISE/NEOWISE, yielding 18 thermal lightcurves. By fitting these data with RSTPM, best-fit spin orientation of Themis is derived to be ($\lambda = 137^\circ$, $\beta = 59^\circ$) in ecliptic coordinates, the mean radius of dust grains on the surface is estimated to be $\tilde{b} = 140^{+500}_{-114}$ (6 ~ 640) μm , indicating the surface thermal inertia to vary from $\sim 3 \text{ Jm}^{-2}\text{s}^{-0.5}\text{K}^{-1}$ to $\sim 60 \text{ Jm}^{-2}\text{s}^{-0.5}\text{K}^{-1}$ due to seasonal temperature variation. Further analysis found that thermal light curves of Themis show a weak rotation-phase dependent feature, indicative of heterogeneous thermal properties or imperfections of lightcurve inversion shape model.

Keywords: Infrared photometry — Small Solar System bodies — Asteroid surfaces — Computational methods

1. INTRODUCTION

In the solar system, there exist numerous small bodies, which are believed to be small planetesimals that did not grow large enough to become planets. Thus some small bodies, especially low-albedo asteroids (e.g. C-types) and fresh comets, should contain primitive materials remaining from the formation of the Solar System, and hence can provide important clues to the composition of the solar nebula in which planets formed, thus improve our understanding of the origin of Solar system.

Temperature distributions of the surface and subsurface layers on small bodies are crucial for the study about thermophysical properties of their surface materials. To obtain the surface and subsurface temperature distributions, we would need a so-called 'surface thermophysical model', which aims to simulate such temperature distributions on the basis of the

realistic physical conditions, including the orbital motion, rotation state, shape topography, surface roughness and surface thermophysical parameters (e.g. thermal inertia).

The first-generation thermophysical models (TPMs) of small bodies, typically like [Spencer \(1990\)](#), [Lagerros \(1996a,b, 1997, 1998\)](#), and [Delbo \(2004\)](#), are mainly designed for the so-called 'radiometric method', which aims to interpret disk-integrated thermal emission observations of asteroids. Due to the limitation of both spatial and time resolution of astronomical instruments at that age, very limited thermal infrared observations could be obtained for few asteroids of interest, causing that we could only estimate the global mean thermal inertias and mean roughnesses of these asteroids. However, the appearance of roughness makes the surface emit in a non-Lambertian way, causing more flux to be observed at low solar phase angles. This effect is known as the "thermal infrared beaming effect" ([Lagerros 1998](#)), which leads to somewhat similar effect as a low thermal inertia surface. Thus parameters of thermal inertia and roughness have inevitable degeneracy in the radiometry procedure. To remove the degeneracy of thermal inertia and roughness, we

would need thermal infrared observations at multiple solar phase angles, namely observations at multiple epoches.

During the past thirty years, thanks to numerous new thermal infrared data of small bodies from space telescopes — IRAS, Spitzer, AKARI and WISE/NEOWISE, and high-precision in-situ thermal infrared imaging from space missions of small bodies — Rosetta, Hayabusa2 and OSIRIS-REx, the requirements of observations at multiple epochs have been well met. Particularly, the WISE/NEOWISE mission has obtained multi-epoch thermal lightcurves of many small bodies. Now with these observations, we are able to remove the degeneracy of thermal inertia and roughness, and simultaneously obtain constraints of their values with the radiometric model. Hence, thermophysical modelling of small bodies has made extraordinary progress in recent years. A review of previous TPMs of small bodies can be found in [Delbo et al. \(2015\)](#), and many updated version of TPMs have been proposed to be applied to specific cases ([Rozitis & Green 2011](#); [Davidsson & Rickman 2014](#); [Hanuš et al. 2015](#)). [Rozitis & Green \(2011\)](#) made progress by modelling thermal emission of rough surface in consideration of shadowing effect, scattering of sunlight and self-heating within the rough region. [Davidsson & Rickman \(2014\)](#) made improvements by considering 3D heat conduction and roughness on spatial scales smaller than the thermal skin depth. [Hanuš et al. \(2015\)](#) further introduced a varied shape TPM scheme, where asteroid shape and pole uncertainties are taken into account.

With these updated TPMs, the “thermal infrared beaming effect” on airless bodies (e.g. Moon, small satellite, asteroids and even comets) can be well explained, and thus the degeneracy of thermal inertia and roughness can be well resolved from the radiometric procedure. However, there still remains problems when we have to explain multi-epoch thermal infrared data from WISE/NEOWISE with the current TPMs:

First, for some small bodies, especially main-belt asteroids, W1-band and W2-band observations of WISE/NEOWISE could contain a significant amount of reflected sunlight. Sunlight reflection is related to the surface albedo and roughness, which also have important influence on the surface thermal emission. How to model sunlight reflection and thermal emission of the surface with unified geometry and physical parameters becomes an important problem.

Second, if a target small body has a large orbital eccentricity or an obliquity close to 90 degrees, it would show significantly different temperature at different epoches, such as (3200) Phaethon in [Yu, Ip & Spohn \(2019\)](#) and (349) Dembowska in [Yu et al. \(2017\)](#). Since thermal parameters including specific heat capacity c and thermal conductivity κ are strong functions of temperature, the value of thermal inertia defined as $\Gamma = \sqrt{\rho c \kappa}$ (ρ means density) is certainly a strong function of temperature as well. Consequently, such small bodies can have significantly different thermal inertias at different epoches (see, for example, [Rozitis et al. 2018](#)). In such cases, a mean thermal inertia derived by the radiometric pro-

cedure may not well represent the thermophysical properties the surface materials.

If there is a dust mantle (regolith layer) on the surface, the specific heat capacity of the dust mantle can be expressed as a function of temperature and material type, while the thermal conductivity can be described as a function of temperature, porosity of dust mantle, density and mean size of dust grains ([Gundlach & Blum 2013](#)). The dust-mantle porosity and dust grain density for small bodies with the same spectral would not be expected to differ very much ([Britt et al. 2002](#)), whereas the mean grain size may be obviously different for various small bodies even if they have similar spectral type. Besides, the mean size of dust grains would be nearly unchanged at each observation epoch. Therefore, for small bodies covered by dust mantle, it may be more appropriate to use mean size of dust grains rather than mean thermal inertia as the free parameter in radiometric procedure.

In this paper, we propose a thermophysical model for realistic surface layers on airless small bodies (RSTPM for short). The model considers not only real shape and rough surface, but also real orbital cycle, rotational cycle, and even temperature dependent thermal parameters in the thermal simulation process, as well as contribution of sunlight reflection in the infrared radiometric procedure. In comparison to previous models, RSTPM differs in three aspects, including: (1) A different mathematical technique is used to solve the influence of surface roughness on the energy balance equation of surface boundary; (2) For the aim to remove the degeneracy of thermal inertia and roughness by interpreting multi-epoch thermal light-curves, variation of thermal parameters due to temperature variation caused by orbital cycle and rotation cycle is taken into consideration; (3) A combination model of simultaneously computing thermal emission and sunlight-reflection under the same surface topography is proposed to fit infrared data in case of the data containing significant sunlight reflection. The structure of the paper is as follows: Section 2 presents the details of the physics and mathematics of RSTPM. Section 3 gives the description of the temperature dependent thermal parameters. Section 4 describes the radiometric procedure. In Section 5, the application of RSTPM to interpret multi-year thermal lightcurves of (24) Themis by WISE/NEOWISE is presented. Finally, Section 6 gives an open discussion and brief conclusion of this model.

2. MODEL DESCRIPTION

2.1. Thermal Diffusion

For any small body in space, we could imagine that, following its rotation as well as orbital movement, the temperature distribution $T(t, \vec{r})$ all over the small body would vary with time, which is dominated by the energy conservation law:

$$\frac{\partial U}{\partial t} + \nabla \cdot \vec{q} = \sum Q_s, \quad (1)$$

where $U = U[T(t, \vec{r})]$ is the density of internal energy, t represents time, \vec{r} means position vector, \vec{q} is the heat flux, and

Q_s represents possible energy production source, such as energy released by the decay of ^{26}Al .

Generally, the so-called specific heat capacity $c(T)$, defined to be the amount of heat required to raise the temperature of unit mass substance by one degree, is introduced as

$$c(T) = \frac{1}{\rho} \frac{\partial U}{\partial T}, \quad (2)$$

so that the first term in Equation (1) can be re-written as

$$\frac{\partial U}{\partial t} = \frac{\partial U}{\partial T} \frac{\partial T}{\partial t} = \rho c_v(T) \frac{\partial T}{\partial t} \text{ or } \rho c_p(T) \frac{\partial T}{\partial t}, \quad (3)$$

in consideration of whether the system is under constant volume ($c_v(T)$) or constant pressure ($c_p(T)$).

For small bodies, the thermal process generally happens under constant pressure. Thus the specific heat capacity at constant pressure $c_p(T)$ should be adopted. In the case of an airless small body, generally no mass transfer happens, thus density ρ should be constant; and no internal heat source, the item $\sum Q_s = 0$ and can be ignored. Then the energy conservation Equation (1) can be rewritten as the general thermal diffusion equation:

$$\rho c_p(T) \frac{\partial T}{\partial t} = -\nabla \cdot \vec{q}. \quad (4)$$

We can describe the shape of a small body with a polyhedron composed of N triangle facets, thus the small body could be divided into numerous tiny voxels in such a way that each voxel could be marked by two number (m, n) , where m means the radial direction towards surface facet m , and n means the n th voxel below the facet. For each voxel, integrating the two side of Equation (4) leads to the following equation:

$$\int \rho c(T) \frac{\partial T}{\partial t} dV = - \int \nabla \cdot \vec{q} dV = \oint \vec{q} \cdot (-d\vec{S}). \quad (5)$$

If the voxel (m, n) is small enough, its temperature can be assumed as constant within the voxel space, then Equation (5) can be discretized as follows:

$$\begin{aligned} \rho c(T) \frac{\delta T}{\delta t} V_{mn} &= \sum_{\alpha} \vec{q}_{\alpha} \cdot \vec{S}_{\alpha} \\ &= \vec{q}_{\perp\uparrow} \cdot \vec{S}_{\perp\uparrow} + \vec{q}_{\perp\downarrow} \cdot \vec{S}_{\perp\downarrow} + \sum_{\alpha} \vec{q}_{\parallel\alpha} \cdot \vec{S}_{\parallel\alpha}, \end{aligned} \quad (6)$$

where V_{mn} is the volume of voxel (m, n) , α stands for a possible voxel adjoined to voxel (m, n) , \vec{S}_{α} represents the cross-section area-vector between the two voxels, \perp stands for radial conduction, and \parallel stands for lateral conduction.

Heat flow between two voxels is the result of spatial gradient of temperature:

$$\vec{q} = -\kappa(T) \nabla T, \quad (7)$$

where $\kappa(T)$ is the so-called thermal conductivity. Thus the component of the heat flux between voxel α and voxel (m, n)

and the corresponding cross-section area-vector could be expressed as

$$\vec{q}_{\alpha} = \kappa(T_{\alpha \sim mn}) \frac{T_{\alpha} - T_{mn}}{\delta h_{\alpha}} \vec{l}_{\alpha \rightarrow mn}, \quad \vec{S}_{\alpha} = S_{\alpha} \vec{n}_{\alpha \rightarrow mn} \quad (8)$$

respectively, where $\vec{l}_{\alpha \rightarrow mn}$ is the unit direction vector from voxel α to voxel (m, n) , $\vec{n}_{\alpha \rightarrow mn}$ represents the unit normal vector, δh_{α} means the average distance between voxel α and voxel (m, n) .

Assume the typical size of a facet in the shape model we utilized is l_{facet} , and the typical thermal penetration depth (generally named as 'thermal skin depth') is l_{st} . Then we can make the following approximations:

$$\delta h_{\perp} \sim l_{\text{st}}, \quad S_{\perp} \sim l_{\text{facet}}^2, \quad \delta h_{\parallel} \sim l_{\text{facet}}, \quad S_{\parallel} \sim l_{\text{st}}^2,$$

$$\frac{S_{\parallel}}{\delta h_{\parallel}} \sim \left(\frac{l_{\text{st}}}{l_{\text{facet}}} \right)^3 \frac{S_{\perp}}{\delta h_{\perp}}. \quad (9)$$

For typical small bodies, l_{facet} ($\sim 10\text{m}$) is far more larger than l_{st} ($\sim 10^{-2}\text{m}$), and

$$\frac{l_{\text{st}}}{l_{\text{facet}}} \sim 10^{-3}, \quad \frac{S_{\parallel}}{h_{\parallel}} \sim 10^{-9} \frac{S_{\perp}}{h_{\perp}},$$

thus the lateral conduction could be sufficiently small to be ignored.

On the other hand, the radial conduction items could be further simplified via the following approximations

$$S_{\perp\uparrow} \sim S_{\perp\downarrow} \sim S_{\perp},$$

$$V_{mn} \sim \delta h S_{\perp},$$

$$\vec{q}_{\perp\uparrow} \cdot \vec{S}_{\perp\uparrow} \sim \kappa(T_{m,n}) \frac{T_{m,n-1} - T_{mn}}{\delta h} S_{\perp},$$

$$\vec{q}_{\perp\downarrow} \cdot \vec{S}_{\perp\downarrow} \sim \kappa(T_{m,n+1}) \frac{T_{m,n+1} - T_{mn}}{\delta h} S_{\perp}.$$

Then Equation (6) could be simplified to be 1D heat conduction equation as

$$\rho c(T) \frac{\delta T}{\delta t} \approx \frac{\vec{q}_{\perp\uparrow} \cdot \vec{S}_{\perp\uparrow} + \vec{q}_{\perp\downarrow} \cdot \vec{S}_{\perp\downarrow}}{V_{mn}} \approx \frac{\delta}{\delta h} \left[\kappa(T) \frac{\delta T}{\delta h} \right], \quad (10)$$

which would be precise enough to model temperature distribution of the surface layers of small bodies. But if l_{st} is comparable to l_{facet} , 3D thermal diffusion model would be necessary.

2.2. Boundary Conditions

For a voxel at the very surface of an airless small body in space, heat flow around this voxel contains, not only conduction between adjoining voxels, but also absorbed incident solar flux and escaped thermal emission flux, thus the conservation of energy gives the surface boundary condition as:

$$\frac{\delta U}{\delta t} = Q_{\text{absorbed}} - Q_{\text{emitted}} + Q_{\text{conduction}} = 0, \quad (11)$$

if considering quasi-equilibrium state.

However, for some small bodies, especially irregular-shape asteroids, (e.g. Eros, Toutatis and so on), the effect from topography and roughness are significant, which are necessary to be considered in the surface boundary condition.

Topography and roughness both indicate the fluctuation of height on the surface. Their difference lies in the spatial scale, where topography refers to a relatively large spatial scale ($>$ tens of meters), which only causes shadow, while roughness refers to a macroscopic small spatial scale (meters), which can cause not only shadow but also multi-scattering of sunlight and self-heating by self-thermal emission.

Therefore, for a small body, if its 3D shape model is composed of ~ 2000 surface elements, the typical size of a facet element l_{facet} can be treated as the spatial scale of topography, while the spatial scale of roughness, say l_{R} , should be much smaller than l_{facet} , but far larger than the thermal skin depth l_{st} ($l_{\text{st}} \ll l_{\text{R}} \ll l_{\text{facet}}$).

If the topography around facet m is significant, probably causing it to be shaded by other facets, then no sunlight will shine into this facet.

If the facet m is a significant rough surface, we can further divide it into several sub-facets, where each sub-facet i is treated as smooth Lambertian surface. Then several significant effects would arise within the sub-facets, such as:

(a). Some sub-facets may be shaded, causing the temperature of these sub-facets to be lower than other sunlit sub-facets. If the small body is observed at zero phase angle, all observed sub-facets would be the hotter ones, but when the observation phase angle deviates from zero, the observed amount of colder sub-facets would significantly increase.

(b). The incident sunlight can be multi-scattered among the sub-facets visible to each other. Thus the total light flux $L(i)$ incident onto the sub-facet i includes not only the light directly from the Sun, but also the scattering light L_{scat} from surrounding visible sub-facets

$$L(i) = L_{\text{s}} v_i \psi_i + L_{\text{scat}}, \quad (12)$$

where $v_i = 1$ indicates that the sub-facet i is visible to the Sun (otherwise $v_i = 0$);

$$\psi_i = \max(\vec{n}_i \cdot \vec{n}_{\odot}, 0), \quad (13)$$

in which \vec{n}_i is the unit normal vector of sub-facet i , and \vec{n}_{\odot} is the unit vector pointing to the opposite direction of sunlight; L_{s} is the integrated solar flux at the distance of the asteroid, which can be approximated by

$$L_{\text{s}} = \frac{L_{\odot}}{d_{\odot}^2},$$

where L_{\odot} is the solar constant, about 1361.5 W m^{-2} , and d_{\odot} is the heliocentric distance in AU. As a result, the effective amount of light energy reflected out from the whole rough surface can be reduced, leading to an effective Bond albedo $A_{\text{eff,B}}$ smaller than the A_{B} of the smooth Lambertian surface.

(c). The sub-facets can absorb thermal radiation R_{th} from surrounding visible facets. As a result, the colder sub-facets can be heated by the hotter ones, this effect is known as the "self-heating effect". So the net thermal flux that escape to the space from a sub-facet i can be written as

$$E_{\text{th}}(i) = \varepsilon \sigma T_i^4 - R_{\text{th}}(i), \quad (14)$$

where T_i represents the temperature of the sub-facet i , ε is the averaged thermal emissivity over the entire emission spectrum of the smooth Lambertian surface, σ is the Stefan Boltzmann constant. As a result, the net fraction of thermal emission energy that escape out to space from the whole rough facet would be reduced.

These effects together contribute to the so-called 'thermal infrared beaming effect' (Lagerros 1998) — the observed disk-integrated flux would significantly decrease when the observation phase angle deviates from zero (Figure 1).

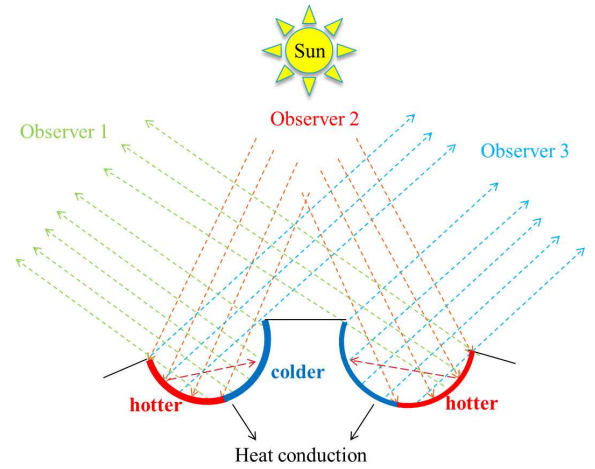


Figure 1. Effects of shadow, multi-scattering, self-heating and beaming on rough surface.

Therefore considering both topography and roughness, the surface boundary condition (11) for a sub-facet on rough surface can be expressed as:

$$(1 - A_{\text{B}})L(i) + R_{\text{th}}(i) - \varepsilon \sigma T_i^4 + \kappa(T) \left. \frac{\delta T}{\delta h} \right|_{h=0} = 0. \quad (15)$$

On the other hand, when there are no internal heat source in the small body, and the small body is large enough so that periodical variation of temperature happens only in the very thin surface layers during the time scale we consider, an isothermal core would form at internal region. Thus the radial temperature gradient below a certain depth would vanish, which gives an internal boundary condition as

$$\left. \frac{\delta T}{\delta h} \right|_{h \rightarrow \infty} \rightarrow 0. \quad (16)$$

2.3. Roughness Representation

In order to quantitatively consider the influence of roughness, we should establish a roughness model to mathematically represent it in the surface boundary condition. A good and widely used way to model the surface roughness (Spencer 1990; Lagerros 1998; Rozitis & Green 2011) is to express it by a fractional coverage of macroscopic bowl-shaped craters, symbolized by f_r ($0 \leq f_r \leq 1$), whereas the remaining fraction, $1 - f_r$, represents a smooth flat Lambertian surface. The configuration of the used macroscopic crater can be described by the depth-to-diameter ratio $\xi = h/D_{\text{rim}} \geq 0$.

The macroscopic crater can be divided into several sub-facets as Figure 2, where each sub-facet is the same as smooth flat Lambertian surface. Then we could use the so-called "root mean square (rms) slope" θ_{rms} to measure the degree of surface roughness. The rms slope is defined as (Spencer 1990)

$$\theta_{\text{rms}} = \sqrt{\frac{\sum_i \theta_i^2 a_i \cos \theta_i}{\sum_i a_i \cos \theta_i}}, \quad (17)$$

where θ_i is the angular slope of facet i to the local horizontal surface, and a_i is the area of facet i . Generally, for a macroscopic spherical crater defined by ξ , its rms slope can be uniquely calculated, like $\theta_{\text{rms}}(\xi)$. Then for a rough surface indicated by a pair of (f_r, ξ) , the RMS slope can be evaluated as

$$\theta_{\text{RMS}}(f_r, \xi) = \sqrt{f_r} \theta_{\text{rms}}(\xi). \quad (18)$$

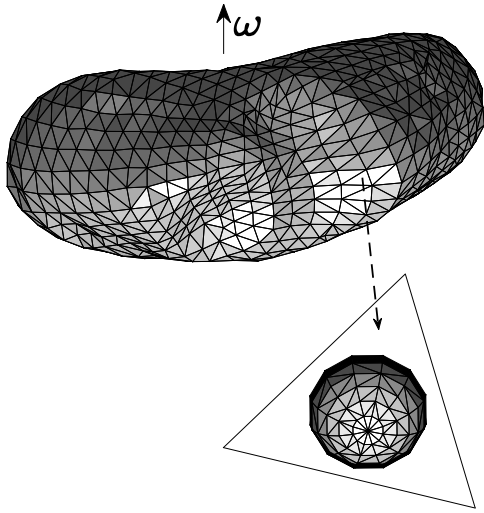


Figure 2. The configuration for a macroscopic crater on a facet of the shape model of (433) Eros. The macroscopic crater is defined with $\xi = 0.5$ and $\theta_{\text{rms}} = 50^\circ$, and is divided into 132 sub-facets.

Typically, for a hemispherical crater defined by $\xi = 0.5$, the rms slope is $\theta_{\text{rms}} = 50^\circ$, while considering $f_r = 0.0 \sim 1.0$, the

surface RMS slope θ_{RMS} is in the range $0 \sim 50^\circ$, decided by the roughness fraction f_r .

2.3.1. Sunlight Multi-scattering

Let's consider a sub-facet i on the rough surface represented by the macroscopic crater shown in Figure 2. If the total light flux incident onto the facet is $L(i)$, then the total light leaving the facet can be expressed $A_B L(i)$, and the scattering light from surrounding visible facets can be estimated via

$$L_{\text{scat}}(i) = \sum_{j \neq i} f(i, j) A_B L(j), \quad (19)$$

where $f(i, j)$ is the so-called "view factor" (Lagerros 1998), meaning the fraction of radiative energy received by facet i to the total radiative energy leaving from facet j , assuming Lambertian energy distribution. Therefore $f(i, j)$ can be expressed as:

$$f(i, j) = \begin{cases} 0, & j = i \\ v_{i,j} a_j \frac{\cos \theta_i \cos \theta_j}{\pi d_{i,j}^2}, & j \neq i \end{cases} \quad (20)$$

where $v_{i,j}$ stands for the fraction of area visible to each other, a_j is the area of facet j , θ_i is the incidence angle on facet i , θ_j is emission angle from facet j , and finally $d_{i,j}$ is the distance between facet i and j . Moreover, for a bowl-shaped crater as showed in Figure 3, we have

$$\cos \theta_i = \cos \theta_j = \frac{0.5 d_{i,j}}{R},$$

thus the view factors can be simplified to be

$$f(i, j) = \begin{cases} 0, & j = i \\ \frac{a_j}{4\pi R^2}, & j \neq i \end{cases} \quad (21)$$

where R is the radius of the sphere, which contains the crater.

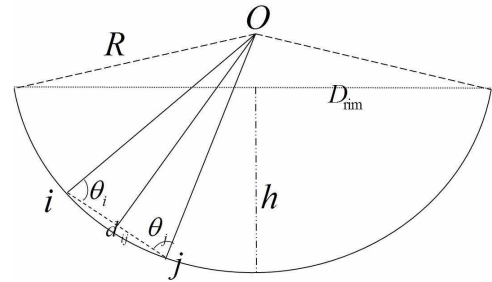


Figure 3. The geometry of a spherical crater ($\xi = h/D_{\text{rim}}$), which is one part of a sphere with radius R . Point O is the centre of the sphere. The rim of the crater has diameter D_{rim} , and the depth is h .

On the other hand, when combining Equation (12) and Equation (19), we can obtain

$$\begin{aligned} L(i) &= L_s v_i \psi_i + \sum_{j \neq i} f(i, j) A_B L(j) \iff \\ L_s v_i \psi_i &= L(i) - \sum_{j \neq i} f(i, j) A_B L(j) = \sum_j \mathbf{A}(i, j) L(j), \end{aligned} \quad (22)$$

where the coefficient matrix $\mathbf{A}(i, j)$ is defined as

$$\mathbf{A}(i, j) = \begin{cases} 1, & j = i, \\ -A_B f(i, j), & j \neq i, \end{cases} \quad (23)$$

being a symmetric matrix. Actually, Equation (22) forms a system of linear equations

$$\mathbf{S} = \mathbf{A} \mathbf{L},$$

where the vector \mathbf{S} has elements $L_s v_i \psi_i$, namely $\mathbf{S}(i) = L_s v_i \psi_i$. The linear Equations can be easily solved by Gauss Elimination Method, giving

$$\mathbf{L} = \mathbf{A}^{-1} \mathbf{S},$$

where \mathbf{A}^{-1} stands for the inverse matrix of \mathbf{A} . Therefore, the actually incident sunlight flux $L(i)$ onto the sub-facet i can be obtained to be

$$L(i) = \sum_j \mathbf{A}^{-1}(i, j) \mathbf{S}(j) = L_s \sum_j \mathbf{A}^{-1}(i, j) v_j \psi_j. \quad (24)$$

2.3.2. Thermal Self-heating

Assume the sub-facet i has temperature T_i , and assume Lambertian emission, then the sub-facet i can absorb the integrated thermal radiation

$$R_{\text{th}}(i) = (1 - A_{\text{th}}) \sum_{j \neq i} f(i, j) \varepsilon \sigma T_j^4 \quad (25)$$

from surrounding visible sub-facets, where A_{th} is the average albedo over the entire thermal emission spectrum, and can be related to ε as $1 - A_{\text{th}} = \varepsilon$ according to the Kirchhoff's law.

Therefore, the surface condition for a sub-facet on rough surface can be further expressed as

$$\begin{aligned} (1 - A_B) L_s \sum_j \mathbf{A}^{-1}(i, j) v_j \psi_j + (1 - A_{\text{th}}) \sum_{j \neq i} f(i, j) \varepsilon \sigma T_j^4 \\ - \varepsilon \sigma T_i^4 + \kappa(T) \frac{\delta T}{\delta h} \Big|_{h=0} = 0. \end{aligned} \quad (26)$$

2.3.3. Average Boundary Condition

If integrate Equation (24) for all sub-facets, the total effective absorbed energy by the macroscopic crater can be approximated as

$$\begin{aligned} (1 - A_{\text{e,B}}) L_s \psi a_{\text{rim}} &= \sum_i (1 - A_B) L(i) a_i \\ &= (1 - A_B) L_s \sum_i \sum_j \mathbf{A}^{-1}(i, j) v_j \psi_j a_i, \end{aligned} \quad (27)$$

where $A_{\text{e,B}}$ stands for the effective Bond albedo of the crater, and the effective sunlit area of the crater equals

$$\psi a_{\text{rim}} = \sum_j v_j \psi_j a_j.$$

Thus we can obtain

$$\begin{aligned} A_{\text{e,B}} &= 1 - (1 - A_B) \frac{\sum_i \sum_j \mathbf{A}^{-1}(i, j) v_j \psi_j a_i}{\sum_j v_j \psi_j a_j} \\ &= 1 - (1 - A_B) \frac{\sum_j \sum_i \mathbf{A}^{-1}(j, i) v_j \psi_j a_j}{\sum_j v_j \psi_j a_j} \\ &\approx 1 - (1 - A_B) \left\langle \sum_i \mathbf{A}^{-1}(j, i) \right\rangle_j, \end{aligned} \quad (28)$$

when the area a_i of the sub-facets are nearly the same. The symbol ' $\langle \rangle_j$ ' represents operation of averaging as

$$\left\langle \sum_i \mathbf{A}^{-1}(i, j) \right\rangle_j = \frac{1}{n} \sum_j \sum_i \mathbf{A}^{-1}(i, j),$$

in which n is the dimension of matrix \mathbf{A} and \mathbf{A}^{-1} .

According to $\mathbf{A} \mathbf{A}^{-1} = \mathbf{I}$ and $\mathbf{A}^T = \mathbf{A}$, we have

$$\left\langle \sum_i \mathbf{A}(i, j) \right\rangle_j \left\langle \sum_i \mathbf{A}^{-1}(j, i) \right\rangle_j = 1. \quad (29)$$

Besides, according to Equation (23)

$$\begin{aligned} \left\langle \sum_i \mathbf{A}(i, j) \right\rangle_j &= \frac{1}{n} \sum_j \sum_i \mathbf{A}(i, j) = 1 - A_B \frac{1}{n} \sum_i \sum_j f(i, j), \\ \frac{1}{n} \sum_i \sum_j f(i, j) &= \frac{1}{n} \sum_i \sum_{j \neq i} \frac{a_j}{4\pi R^2} \approx \frac{1}{4\pi R^2} \sum_j a_j \\ &= \frac{2\pi R h}{4\pi R^2} = \frac{4\xi^2}{1 + 4\xi^2}. \end{aligned} \quad (30)$$

Therefore,

$$\left\langle \sum_i \mathbf{A}^{-1}(j, i) \right\rangle_j = 1 / \left\langle \sum_i \mathbf{A}(i, j) \right\rangle_j = \frac{1}{1 - A_B \frac{4\xi^2}{1 + 4\xi^2}},$$

$$\begin{aligned} A_{\text{e,B}} &\approx 1 - (1 - A_B) \left\langle \sum_i \mathbf{A}^{-1}(j, i) \right\rangle_j \\ &\approx 1 - \frac{(1 - A_B)}{1 - A_B \left(\frac{4\xi^2}{1 + 4\xi^2} \right)} \\ &= \frac{A_B}{1 + 4\xi^2(1 - A_B)}, \end{aligned} \quad (31)$$

and finally the averaged effective Bond albedo of a rough surface defined by (f_r, ξ) can be evaluated as

$$A_{\text{eff,B}} = (1 - f_r) A_B + f_r \frac{A_B}{1 + 4\xi^2(1 - A_B)}. \quad (32)$$

On the other hand, from the point of view of energy conservation, we could define an effective temperature T and effective thermal emissivity ε_e for the macroscopic crater via

$$T^4 = \frac{1}{a_{\text{rim}}} \sum_i T_i^4 a_i, \quad \varepsilon_e = \frac{E_c}{\sigma T^4 a_{\text{rim}}}, \quad (33)$$

where E_c is the net thermal emission energy escaping out from the whole crater

$$E_c = \sum_i E_{\text{th}}(i) a_i = \sum_i (\varepsilon \sigma T_i^4 - R_{\text{th}}) a_i. \quad (34)$$

Then the effective thermal emissivity ε_e can be derived to be

$$\begin{aligned} \varepsilon_e &= \left(1 - \frac{\sum_i a_i \sum_{j \neq i} (1 - A_{\text{th}}) \frac{a_j}{4\pi R^2} \sigma T_j^4}{\sum_i \sigma T_i^4 a_i} \right) \varepsilon \\ &\approx \left(1 - \frac{(1 - A_{\text{th}}) \sum_i a_i}{4\pi R^2} \right) \varepsilon \\ &= \frac{1 + 4\xi^2 A_{\text{th}}}{1 + 4\xi^2} \varepsilon, \end{aligned} \quad (35)$$

and the averaged effective thermal emissivity of a rough surface defined by (f_r, ξ) can be evaluated as

$$\varepsilon_{\text{eff}} = (1 - f_r) \varepsilon + f_r \frac{1 + 4\xi^2 A_{\text{th}}}{1 + 4\xi^2} \varepsilon. \quad (36)$$

Therefore, in a view of energy conservation for the whole rough facet, integrate the boundary condition Equation (15) for all sub-facets, and use the averaged effective Bond albedo $A_{\text{eff,B}}$ (Equation 32) as well as the averaged effective thermal emissivity ε_{eff} (Equation 36), we could obtain the average boundary condition of the rough surface as

$$(1 - A_{\text{eff,B}}) L_s \psi - \varepsilon_{\text{eff}} \sigma T^4 + \kappa(T) \frac{\delta T}{\delta h} \Big|_{h=0} = 0, \quad (37)$$

which can be applied in the cases that we do not need to distinguish the temperature difference within the rough facet.

2.4. Standard Transformation

In order to simplify the solution of the above equations, it is useful to introduce a standard transformation as follows:

$$u = \frac{T}{T_*}, \quad \tau = \frac{t}{t_*}, \quad x = \frac{h}{h_*}, \quad (38)$$

where t_* represents the typical time scale of the thermal variation, h_* represents the spatial scale of thermal diffusion, T_* represent the typical temperature of the system during the thermal process.

Then, the 1D heat conduction Equation (10) can be transformed as

$$f_c(u) \frac{\delta u}{\delta \tau} = \frac{\delta}{\delta x} \left[f_\kappa(u) \left(\frac{\alpha_* t_*}{h_*^2} \right) \frac{\delta u}{\delta x} \right], \quad (39)$$

where

$$\alpha_* = \frac{\kappa_*}{\rho c_*}, \quad f_\kappa(u) = \frac{\kappa(T)}{\kappa_*}, \quad f_c(u) = \frac{c(T)}{c_*},$$

in which κ_* and c_* are the reference constant thermal conductivity and heat capacity introduced via

$$\kappa_* = \kappa(T_*), \quad c_* = c(T_*).$$

The thermal state in the surface layers can change cyclically due to the variation of solar insolation caused by some kind of short-term cycle of motion, for example diurnal cycle or seasonal cycle. For such thermal cycles, generally we choose

$$t_* = \frac{1}{\omega},$$

where ω is the rotational angular frequency or orbital angular frequency, and use the so-called thermal skin depth l_{st*} as h_*

$$h_* = l_{st*} = \sqrt{\alpha_* t_*} = \sqrt{\frac{\kappa_*}{\rho c_* \omega}}. \quad (40)$$

And then the 1D heat conduction Equation (39) can be simplified as

$$f_c(u) \frac{\delta u}{\delta \tau} = \frac{\delta}{\delta x} \left[f_\kappa(u) \frac{\delta u}{\delta x} \right]. \quad (41)$$

In realistic cases, both rotation and orbital motion can cause temperature variation. Rotation effect is more important on low-latitude regions, especially on equatorial regions, but none such effect on polar regions. However, if the small body has significant orbital eccentricity and axial tilt, then seasonal thermal variation would become important, especially for high-latitude regions, and even dominates the temperature variation on polar regions.

2.4.1. Diurnal cycle

For diurnal cycle, it is convenient to use the sub-solar temperature T_{ss} as T_*

$$T_* = T_{\text{ss}} = \left[\frac{(1 - A_{\text{eff,B}}) L_s}{\varepsilon \sigma} \right]^{1/4}, \quad (42)$$

then the boundary condition Equation (26) of the rough surface can be converted into

$$\begin{aligned} &\left(\frac{1 - A_{\text{B}}}{1 - A_{\text{eff,B}}} \right) \sum_j \mathbf{A}^{-1}(i, j) v_j \psi_j + \sum_{j \neq i} \varepsilon f(i, j) u_j^4 \\ &= u_i^4 - \Phi_* f_\kappa(u) \frac{\delta u}{\delta x} \Big|_{x=0}, \end{aligned} \quad (43)$$

where

$$\Phi_* = \frac{\Gamma_* \sqrt{\omega}}{\varepsilon \sigma T_c^3}, \quad (44)$$

is the characteristic thermal parameter, in which

$$\Gamma_* = \sqrt{\rho c_* \kappa_*}$$

is the corresponding characteristic thermal inertia.

where

$$a_j = \begin{cases} 0, & j = 1 \\ -f_{i,j-1}, & j = 2, N-1 \\ 1, & j = N \end{cases}$$

$$b_j = \begin{cases} 1, & j = 1 \\ 1 + f_{i,j-1} + f_{i,j}, & j = 2, N-1 \\ -1, & j = N \end{cases}$$

$$c_j = \begin{cases} 0, & j = 1 \\ -f_{i,j}, & j = 2, N-1 \\ 0, & j = N \end{cases}$$

$$d_j = \begin{cases} BC(p_1, p_2), & j = 1 \\ f_{i,j-1}u_{i,j-1} + (1 - f_{i,j-1} - f_{i,j})u_{i,j} + f_{i,j}u_{i,j+1}, & j = 2, N-1 \\ 0, & j = N \end{cases}$$

Equation (53) is still a nonlinear equation, because the coefficients contain the temperature dependent function $f_{i,j}$. To solve this kind of nonlinear heat conduction equation, we could use the so-called 'predictor-corrector' method, which is a two-step iterative procedure. The advance from temperature u at current time τ to temperature u^n at next time $(\tau + \delta\tau)$ is implemented through the temperature $u^{n-1/2}$ at a intermediate time step $(\tau + \delta\tau/2)$.

Firstly, the *predictor* step, we can obtain the intermediate temperature $u^{n-1/2}$ from the current temperature u by taking the coefficient $f_{i,j}(u)$ with current temperature u .

Secondly, the *corrector* step, the coefficients $f_{i,j}(u^{n-1/2})$ are derived by the temperature $u^{n-1/2}$ at time step $(\tau + \delta\tau/2)$, so as to obtain u^n from u .

Both the *predictor* and *corrector* step need the solution of the linear tridiagonal system of equations, which already has known solution algorithms.

3. THERMAL PARAMETERS

3.1. Specific heat capacity

The specific heat capacity of simple materials as a function of temperature can be described by the Debye's theory when the temperature is not very high (lower than the so-called Debye characteristic temperature). But for materials on planetary surface or minerals, the relation between specific heat capacity and temperature actually deviates from the Debye's theory. Nevertheless, the positive correlation that specific heat capacity increases with the increasing of temperature is similar to the Debye's formula. Hence, the Debye's formula can serve as an approximation for the temperature dependence of specific heat capacity of minerals or planetary surface materials.

Considering that the Debye's formula of specific heat capacity is a time-consuming integration formula, here we present a simplified formula to approximate the positive correlation between specific heat capacity and temperature

based on the Debye's formula:

$$c_v(T) = \frac{3k_B}{m_a} \left\{ \frac{a\left(\frac{T}{T_D}\right)^3 \left[a\left(\frac{T}{T_D}\right)^3 + 2b\left(\frac{T}{T_D}\right)^2 + 3c\frac{T}{T_D} + 4 \right]}{\left[a\left(\frac{T}{T_D}\right)^3 + b\left(\frac{T}{T_D}\right)^2 + c\frac{T}{T_D} + 1 \right]^2} \right\}, \quad (54)$$

where the coefficients

$$a \approx 39.09, b \approx 14.46, c \approx 3.304,$$

k_B is the Boltzmann's constant, $m_a = \rho/n$ is the average atom mass of the material, and T_D is a "characteristic temperature" of the material that would be measured by experiments.

While we have no exact information about surface materials on small bodies, we may find their most spectral-resembled chondrites to estimate their heat capacities. The average atom mass m_a of several chondrites are listed in Table 1.

Table 1. The average atom mass m_a of known chondrites according to composition of chondrites given by Wasson & Kallemeyn (1988).

chondrite	m_a
Type	($1.66053873 \times 10^{-27}$ kg)
CI	21.5515
CM	22.7817
H	24.9229
L	23.6574
LL	23.4194
EH	25.9846
EL	25.1344

In principle, the characteristic temperature T_D of each chondrite can be obtained by fitting experimental data of specific heat capacities with Equation (54). By comparing Equation (54) with the experimental data of Macke et al. (2016); Opeil & Britt (2016), we suggest a constant

$$T_D \approx 700 \text{ K}$$

for various chondrites.

When the temperature gets very high, the Debye's theory is no longer suitable. Waples & Waples (2004) presents empirical formula for the specific heat capacities of minerals and nonporous rocks at high temperature, where a relative heat capacity is given as

$$N_{cp}(T) = 0.716 + 1.72 \times 10^{-3}(T - 273.4) - 2.13 \times 10^{-6}(T - 273.4)^2 + 8.95 \times 10^{-10}(T - 273.4)^3, \quad (55)$$

and the specific heat capacity is then estimated via

$$c_p(T) = c_p(T_0) \frac{N_{cp}(T)}{N_{cp}(T_0)}. \quad (56)$$

Then the variation of specific heat capacity in a very large temperature scale can be expressed as

$$c_p(T) = \begin{cases} c_v(T), & T < 300K, \\ c_v(300) \frac{N_{cp}(T)}{N_{cp}(300)}, & T \geq 300K. \end{cases} \quad (57)$$

Here in Figure 4, we present the specific heat capacities of CI, CM, H, L, LL chondrites obtained by the above methods.

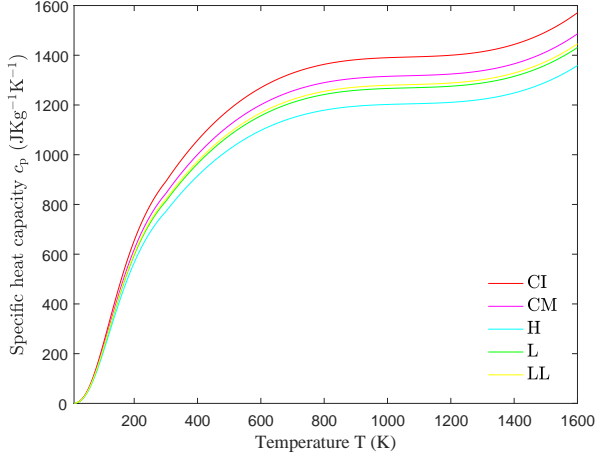


Figure 4. Model results of specific heat capacities of CI, CM, H, L, LL chondrites.

3.2. Thermal conductivity

For small bodies covered by dust mantle, the thermal conductivity κ of the dust mantle can be related to the temperature T , mean radius b of grains and dust mantle porosity ϕ via the model of Gundlach & Blum (2013):

$$\kappa(T, b, \phi) = \kappa_{\text{solid}} \left(\frac{9\pi}{4} \frac{1 - \mu^2}{E} \frac{\gamma(T)}{b} \right)^{1/3} \chi f_1 e^{f_2(1-\phi)} + 8\sigma\epsilon T^3 \frac{e_1\phi}{1-\phi} b. \quad (58)$$

The details of Equation (58) are described in Gundlach & Blum (2013).

Based on Equation (58), in Figure 5, we show how the thermal conductivities change with temperature for C-type and S-type asteroids, assuming mean grain radius $b = 0.5$ mm, porosity $\phi = 0.5$.

3.3. Thermal inertia

As shown in Figure 4 and Figure 5, both the specific heat capacities and thermal conductivities are strong functions of temperature, thus the so-called thermal inertia

$$\Gamma = \sqrt{\rho c_p \kappa}, \quad (59)$$

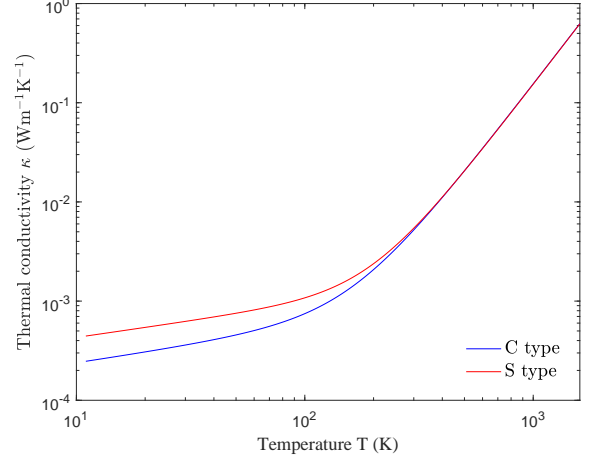


Figure 5. Temperature dependent thermal conductivities of C-type and S-type asteroids, assuming mean grain radius $b = 0.5$ mm, porosity $\phi = 0.5$.

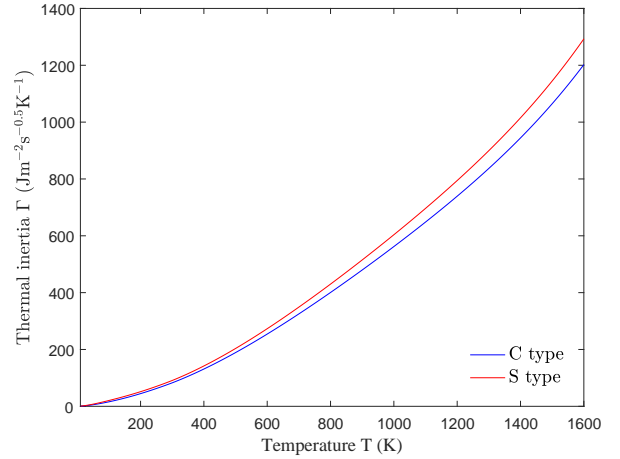


Figure 6. Temperature dependent thermal inertias of C-type (CM) and S-type (LL) asteroids, assuming mean grain radius $b = 0.5$ mm, surface porosity $\phi = 0.5$, grain density 3100 kg m^{-3} for C-type but 3700 kg m^{-3} for S-type.

is also strongly temperature dependent (seeing Figure 6).

According to the surface boundary condition Equation (43), the thermal parameter that relates to thermal inertia decides how the surface temperature changes. The thermal inertia, as indicated by its name, generally implies the ability to maintain the thermal state. Thus, the larger thermal inertia is, the slower temperature variation would be, and probably causing significant thermal-delay effect, generating asymmetric temperature distribution between the sunrise side and the sunset side.

On the other hand, due to the strong positive correlation between thermal inertia and temperature, the rise of temperature could increase thermal inertia, and thus slow down the temperature increase and enhance the thermal delay ef-

fect, while inversely, the decline of temperature would reduce thermal inertia, and thus promote the temperature decrease. As a result, temperature distribution between the sunrise and the sunset sides would tend to be even more asymmetric due to the temperature dependence of the thermal parameter.

In the following sub-sections, we will use RSTPM to show how the temperature dependence of thermal inertia enhances the asymmetry of temperature distribution in the diurnal cycle of small bodies. As examples, let's consider S-type asteroids at 1 AU from the Sun and physical parameters listed in Table 2.

Table 2. Assumed parameters for the test asteroids.

Properties	Value
Heliocentric distance	1 AU
Rotation obliquity	0°
Rotation period P_R	10 hr
Roughness fraction f_r	0.0
Bond albedo A_B	0.04
Thermal emissivity ε	0.9
Resembled chondrite	LL
Material density ρ_m	3700 kgm ⁻³
Surface porosity ϕ	0.5

3.3.1. Mean Thermal inertia vs Mean grain radius

As a comparison to the realistic case, firstly we have to define a constant mean thermal inertia, which ignores the temperature dependence. Therefore, we need a mean temperature \tilde{T} , and the mean thermal inertia is defined as

$$\tilde{\Gamma} = \sqrt{\rho c_p(\tilde{T})\kappa(\tilde{T})}. \quad (60)$$

For the test asteroids with above conditions, the diurnal mean temperature on the equator can be estimated to be

$$\tilde{T} = \left(\frac{(1 - A_B)L_\odot}{\varepsilon\sigma\pi} \right)^{1/4} \approx 300 \text{ K}.$$

Then the mean grain radius \tilde{b} would be the main parameter that decides the mean thermal inertia $\tilde{\Gamma}$ as shown in Figure 7, which shows that larger grain radius generally means larger thermal inertia.

3.3.2. Enhanced Asymmetric Temperature Distribution

In Figure 8, we show the diurnal temperature variation obtained by two models with different thermal parameters. The solid curves (with color in red, green and blue) are obtained by RSTPM, considering temperature dependent thermal parameters in three cases of mean grain radius

$$\tilde{b} = 0.1, 1, 10 \text{ mm}$$

respectively, while the dotted curve with the same color are obtained by Commonly used Thermophysical Models (using

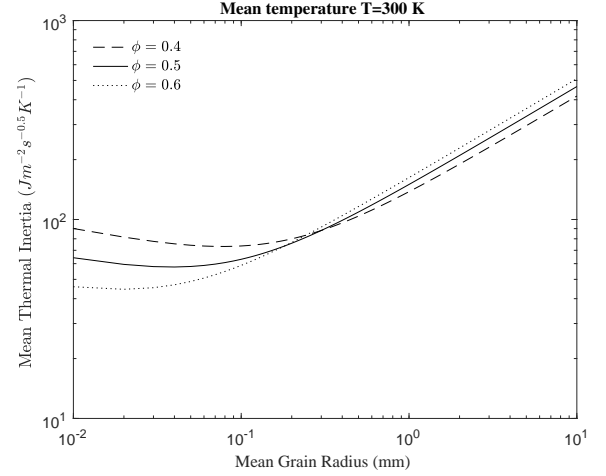


Figure 7. The relation of mean thermal inertia and mean grain radius under the condition given in Table 2

CTPM for short) that ignores temperature dependence, using the corresponding mean thermal inertia

$$\tilde{\Gamma} = 63, 150, 466 \text{ Jm}^{-2}\text{s}^{-0.5}\text{K}^{-1}$$

respectively.

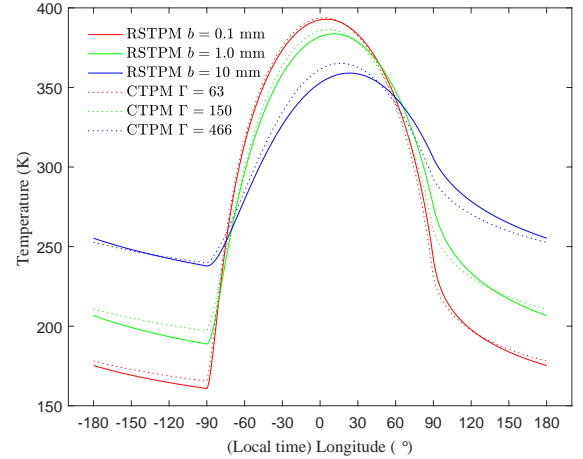


Figure 8. Modeled diurnal temperature variation with two different models: RSTPM (solid curves), the model presented in this work, considers temperature dependent parameters when mean grain radius $b = 0.1, 1, 10$ mm respectively; CTPM (dotted curves), a common used thermophysical model, ignoring temperature dependence, considers constant thermal inertia $\Gamma = 63, 150, 466 \text{ Jm}^{-2}\text{s}^{-0.5}\text{K}^{-1}$ (red solid curve) respectively.

Firstly, if we do comparisons between curves with different color, we can see that larger thermal inertia tends to generate stronger thermal delay effect or asymmetric temperature distribution.

Secondly, if we do comparisons between the solid curves and the corresponding dotted curves with the same color, the

temperature distribution tends to be more asymmetric if thermal parameters' temperature dependence is taken into consideration. Such effect can lead to a temperature difference as large as ~ 10 K, which can hence induce variation of thermal emission within

$$\sim \left(\frac{300 + 10}{300} \right)^4 \sim 14\%.$$

Finally, the asymmetry enhancement tends to be more significant for cases with larger thermal inertia (blue curves).

4. THERMAL INFRARED RADIOMETRY

The infrared radiation from a small body is related to its size as well as temperature distribution, which is decided by the surface thermophysical properties (e.g. albedo, roughness and thermal inertia). Thus these properties could be well determined by fitting the measurements of its infrared radiation with the surface thermophysical model. This procedure is known as the so-called "Thermal Infrared Radiometry". However, for any body except the Sun in the solar system, the observed infrared radiation is the integration of its own thermal emission and the reflected sunlight, especially radiation at wavelength $< 5 \mu\text{m}$, containing significant fraction of sunlight (e.g. W1 and W2 band of WISE/NEOWISE, see Figure 21 in Section 5.4). Thus both thermal emission and sunlight reflection should be taken into account in the radiometric model.

4.1. Disk-integrated thermal emission

On the basis of the previously described roughness model, we treat the facet i of the shape model and the sub-facet j in the crater on facet i both to be smooth Lambertian surface, and hence thermal radiation from them can be approximated by Lambertian radiation. So for a given epoch with a certain observation phase angle α and distance Δ , thermal emission from facet i and sub-facet ij that can be observed by the telescope will be $\epsilon(\lambda)\pi B_i f_i$ and $\epsilon(\lambda)\pi B_{ij} f_{ij}$, where $\epsilon(\lambda)$ is the monochromatic emissivity at wavelength λ , f_i and f_{ij} are the view factors of facet i and sub-facet ij relative to the telescope, B_i and B_{ij} are Planck intensity function on a temperature T_i and T_{ij}

$$B(\lambda, T_i) = \frac{2hc^2}{\lambda^5} \frac{1}{\exp\left(\frac{hc}{\lambda k T_i}\right) - 1}. \quad (61)$$

The so-called view factor f_i is defined as

$$f_i = v_i a_i \frac{\vec{n}_i \cdot \vec{n}_{\text{obs}}}{\pi \Delta^2}, \quad (62)$$

where a_i and \vec{n}_i are the area and normal vector of facet i , \vec{n}_{obs} is the unit vector of the telescope's direction in the body-fix coordinate system, $v_i = 1$ indicates that facet i is observable from the telescope, otherwise $v_i = 0$.

With the temperature distribution T_i and T_{ij} computed from the above numerical method, the observable thermal

emission F_{th} of the entire small body can be expressed as the integration of thermal emission from both the smooth and rough surface:

$$F_{\text{th}}(\lambda) = (1 - f_r) \sum_{i=1}^N \epsilon(\lambda)\pi B_i f_i + f_r \sum_i^N \sum_j^M \epsilon(\lambda)\pi B_{ij} f_{ij}. \quad (63)$$

4.2. Disk-integrated sunlight reflection

While it could be a good approximation to calculate the absorption of solar energy by assuming Lambertian surface, such approximation will not be good enough if we care about the exact reflected sunlight. Actually, sunlight reflection by realistic planetary surface deviates largely from the ideal Lambertian reflection, due to multiple effects including asymmetric scattering by irregular-shape dust particles and macroscopic-roughness (far larger than dust particle size) induced beaming effect. The macroscopic roughness model can be similar to the thermal roughness model above. To consider asymmetric scattering, we use the combined Lambert-Lommel-Seeliger law that introduce a correction coefficient C_L to the Lambertian reflection as

$$C_L(\psi_i, \psi_{o,i}, \alpha, w_f) = f(\alpha) \left(w_f + \frac{1}{\psi_i + \psi_{o,i}} \right), \quad (64)$$

where ψ_i and $\psi_{o,i}$ are the cosines of the incident angle and emergence angle on facet i respectively, α is the solar phase angle; $f(\alpha)$ is the phase correction function, according to (Kaasalainen, Torppa & Muinonen 2001),

$$f(\alpha) \sim 0.5 \exp(-\alpha/0.1) - 0.5\alpha + 1.$$

Parameter w_f represents the weight of Lambertian term in the scattering law, so we name it "scattering weight-factor". To ensure $0 \leq C_L \leq 1$, the scattering weight-factor w_f is required to be $0 \leq w_f \leq 0.5$. The value w_f can be determined by doing optimization fitting to observations of sunlight reflection.

Hence, for a given epoch with a certain observation phase angle α and distance Δ , the reflection of sunlight from facet i and sub-facet ij can be expressed as:

$$F_{\text{rl},i}(\lambda) = \pi B(\lambda, 5778) \frac{R_{\text{sun}}^2}{r_{\text{helio}}^2} \cdot A_b(\lambda) \cdot \psi_i \cdot f_i \cdot C_L, \quad (65)$$

$$F_{\text{rl},ij}(\lambda) = \pi B(\lambda, 5778) \frac{R_{\text{sun}}^2}{r_{\text{helio}}^2} \cdot A_b(\lambda) \cdot \psi_{ij} \cdot f_{ij} \cdot C_L, \quad (66)$$

where ψ_i and ψ_{ij} are the cosine values of the solar altitudes, R_{sun} is the radius of the Sun, r_{helio} nearly equals to the heliocentric distance of the asteroid, $B(\lambda, T)$ is the Planck intensity function, and $A_b(\lambda)$ is the albedo at wavelength λ .

Then the total reflected sunlight that can be observed by the telescope is the integration of reflection from all observable facets:

$$F_{\text{rl}}(\lambda) = (1 - f_r) \sum_i^N F_{\text{rl},i} + f_r \sum_i^N \sum_j^M F_{\text{rl},ij}. \quad (67)$$

And the total radiation flux that can be observed by the telescope at wavelength λ would be the sum of thermal emission and sunlight reflection:

$$F_{\text{model}}(\lambda) = F_{\text{th}}(\lambda) + F_{\text{r}}(\lambda). \quad (68)$$

4.3. Thermal Infrared Beaming effect

As mentioned in section 2.2, the appearance of roughness could lead to the so-called thermal infrared beaming effect, making the observed disk-integrated emission flux to decrease significantly when the observation phase angle deviates from zero. Here we use RSTPM to investigate the beaming effect. As an example, a testing asteroid with parameters listed in Table 2 and two cases of roughness fraction $f_r = 0$ and 1.0 are investigated.

In Figure 9, we show the modelled $12 \mu\text{m}$ observation flux in a equatorial view but at various solar phase angle. The observation distance is fixed at 1 AU, but different grain radius are taken into account.

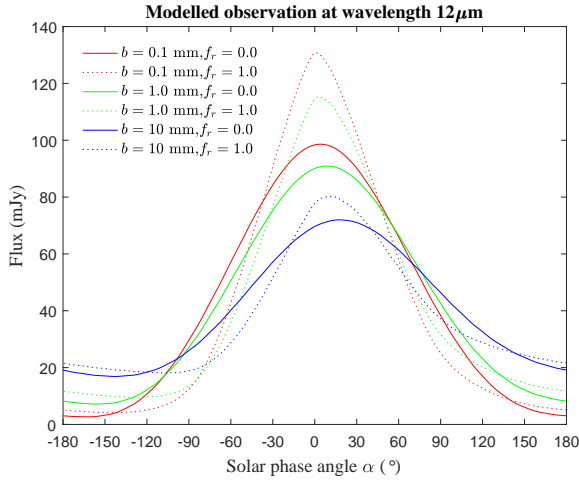


Figure 9. Modelled $12 \mu\text{m}$ observation flux in a equatorial view but at various solar phase angle for a test asteroid with parameters listed in Table 2. The observation distance is fixed at 1 AU, but two roughness fraction $f_r = 0$ and 1.0 and three grain radius $b = 0.1, 1,$ and 10 mm are taken into account.

Firstly, the difference between the dotted curve and the solid curve with the same color clearly reveals the mentioned beaming effect — more emission at zero solar phase angle.

Secondly, the beaming effect tends to be more significant for the cases of low-thermal inertia cases (smaller grain size). The observed flux at zero solar phase can increase up to $\sim 30\%$ (compare the red dotted curve and the red solid curve) due to the beaming effect generated by a totally rough surface (roughness fraction = 1.0).

Thirdly, both the decreasing of thermal inertia and the increasing of roughness can lead to the tendency of emitting more photons at zero solar phase angle. These two effects can be degenerate for observations at insufficient solar phase angles. Therefore, in order to reduce the degeneracy of the

surface thermal inertia and roughness from thermal infrared observations, observations at various solar phase angles are necessary.

4.4. Radiometric Procedure

In order to reproduce the disk-integrated infrared observation of a small body with the RSTPM, we need its 3D shape model, rotation parameters (rotation period and rotation axis orientation), effective diameter D_{eff} , bond albedo A_B , emissivity, and thermophysical parameters ρ, c_p, κ .

4.4.1. Shape Model and Spin orientation

The 3D shape model and spin state can be constructed by the light-curve inversion method developed by Kaasalainen & Torppa (2001) if we have observed enough light-curves, or by inversion of radar Delay-Doppler images (Ostro et al. 2002). Since observations of radar Delay-Doppler images are more difficult than light-curve observations, light-curve inversion method has become the most common-used method to derive shape and spin state of most small bodies. However, even for light-curve observation, it is difficult to obtain enough light-curves to constrain a unique spin orientation for many small bodies. It is fortunate that WISE/NEOWISE have observed lots of thermal lightcurves of many small bodies, among which spin orientation still has different solutions. Therefore, by interpreting the thermal lightcurves of WISE/NEOWISE, it is possible to constrain the spin orientation to a unique solution.

4.4.2. Size and Albedo

According to Fowler & Chillemi (1992), an asteroid's effective diameter D_{eff} , defined by the diameter of a sphere with the same area to that of the shape model, can be related to its geometric albedo p_v and absolute visual magnitude H_v via:

$$D_{\text{eff}} = \frac{1329 \times 10^{-H_v/5}}{\sqrt{p_v}} \text{ (km)}. \quad (69)$$

In addition, the geometric albedo p_v is related to the effective Bond albedo $A_{\text{eff,B}}$ by

$$A_{\text{eff,B}} = p_v q_{\text{ph}}, \quad (70)$$

where q_{ph} is the phase integral that can be approximated by

$$q_{\text{ph}} = 0.290 + 0.684G, \quad (71)$$

in which G is the slope parameter in the H, G magnitude system of Bowell et al. (1989), which can be obtained by photometric observation.

4.4.3. Roughness Fraction

On the other hand, the asteroid's effective Bond albedo is the averaged result of both the albedo of smooth and rough surface, which can be expressed as the following relationship according to Equation (32) ($\xi = 0.5$ for hemispherical crater):

$$A_{\text{eff,B}} = (1 - f_r)A_B + f_r \frac{A_B}{2 - A_B}, \quad (72)$$

where A_B is the Bond albedo of smooth Lambertian surface. Thus an input roughness fraction f_r and geometric albedo p_v can lead to a unique Bond albedo A_B and effective diameter D_{eff} to be used to fit the observations.

4.4.4. Thermal emissivity

We can use the bond albedo A_B to approximate the reflectance $A_b(\lambda)$ at an observation wavelength λ , so as to calculate the reflect sunlight at wavelength λ . On the other hand, according to Kirchhoff's law, the monochromatic emissivity $\epsilon(\lambda)$ at wavelength λ can be approximatively related to $A_b(\lambda)$ via

$$\epsilon(\lambda) = 1 - A_b(\lambda),$$

thus enabling the computation for the thermal emission at wavelength λ . Under such approximation, the size, albedo and emissivity are related to each other, thus becoming one free parameter in the fitting procedure.

4.4.5. Mean Thermal inertia

For the thermophysical parameters, as a first approximation, we may ignore their temperature dependence, and assume a mean thermal inertia of the whole surface to obtain a corresponding mean thermal parameter

$$\tilde{\Phi} = \frac{\tilde{\Gamma} \sqrt{\omega}}{\epsilon \sigma T_e^3}, \quad (73)$$

then we are able to obtain the surface temperature distribution to fit the thermal infrared observations.

Thus we actually have three free parameters — mean thermal inertia, roughness fraction, and geometric albedo (or effective diameter) that would be extensively investigated in the fitting process. We use the so-called reduced χ_r^2 defined as

$$\chi_r^2 = \frac{1}{n-3} \sum_{i=1}^n \left[\frac{F_{\text{model}}(\lambda_i, w_f, p_v, f_r, \tilde{\Gamma}) - F_{\text{obs}}(\lambda_i)}{\sigma_{\lambda_i}} \right]^2, \quad (74)$$

to assess the fitting degree of model results with respect to the observations. The input parameters that gives the minimum χ_r^2 could be treated as the most possible values of these parameters.

4.4.6. Mean Grain radius

Considering that the surface temperature could differ largely at different region and thermal inertia is strongly temperature dependent, the obtained mean thermal inertia from the above radiometry process may not well reveal the physical condition of the surface materials. Thus it is necessary to remove the temperature effect so as to find the more basic properties that is not affected by temperature.

As mentioned in above section, if we know the taxonomic type of a small body from spectral observation, we could find its most spectral-resembled chondrite to estimate the specific heat capacity $c_p(T)$ at various temperature.

Moreover, its surface mass density can also be estimated via

$$\rho = (1 - \phi)\rho_m, \quad (75)$$

where the material density ρ_m can be approximated as the density of the corresponding chondrite, such as (Opeil et al. 2010)

$$\rho_m = 3110 \text{ kgm}^{-3} \text{ for C - type,}$$

$$\rho_m = 3700 \text{ kgm}^{-3} \text{ for S - type,}$$

and the porosity ϕ can have values from 0.4 to 0.6 for the surface layers of airless bodies.

Finally, if the surface is covered by dust mantle, the thermal conductivity can be related to the mean grain radius b like Equation (58), meaning that b would be mainly important free parameter that decides the realistic thermal inertia.

Then we can investigate the three free parameters — mean grain radius, roughness fraction, and geometric albedo (or effective diameter) in the fitting process. Still we use the so-called reduced χ_r^2 defined as

$$\chi_r^2 = \frac{1}{n-3} \sum_{i=1}^n \left[\frac{F_{\text{model}}(\lambda_i, w_f, p_v, f_r, \tilde{b}) - F_{\text{obs}}(\lambda_i)}{\sigma_{\lambda_i}} \right]^2, \quad (76)$$

to assess the fitting degree of model results with respect to the observations. The input parameters that gives the minimum χ_r^2 could be treated as the most possible values of these parameters.

5. APPLICATION EXAMPLE

As an example, we apply RSTPM to study the main belt object (24) Themis, which has been believed to be the parent body of most currently known main-belt comets (MBCs), and hence should have a dust mantle on the surface. MBCs are so small that observations of them are difficult to obtain, whereas Themis is bright enough to be observed at both optical and infrared bands. So using thermal infrared observations to study surface dust properties would be easier for Themis, the results of which can be served as a reference for the surface dust properties of MBCs regarding their possible connections.

Although light-curve observations of Themis have been obtained to derive its spin orientation together with shape model by the light-curve inversion method, there is still no unique solution to the spin orientation as yet. Currently there exist four different solutions to the spin orientation and shape model of Themis, as shown in Table 3 and Figure 10. The lucky thing is that WISE/NEOWISE has got multi-epoch thermal lightcurves of Themis, thus enabling us to find out which of the four shape models is the best by using RSTPM to fit these thermal lightcurves.

5.1. WISE/NEOWISE observation

The *Wide-field Infrared Survey Explorer* (WISE) mission has mapped entire sky in four bands at 3.4 (W1), 4.6 (W2),

Table 3. Light-curve inversion shape models of (24) Themis (Hanuš et al. 2016; Viikinkoski et al. 2017). The shape models can be obtained from the Database of Asteroid Models from Inversion Techniques.

	Spin Orientation (λ, β) (°)	Number of Vertices	Number of Facets
shape 1	(331, 52)	1018	511
shape 2	(137, 59)	1018	511
shape 3	(139, 71)	800	402
shape 4	(329, 70)	800	402

λ : Ecliptic Longitude; β : Ecliptic Latitude.

Spin period: 8.374187 hr

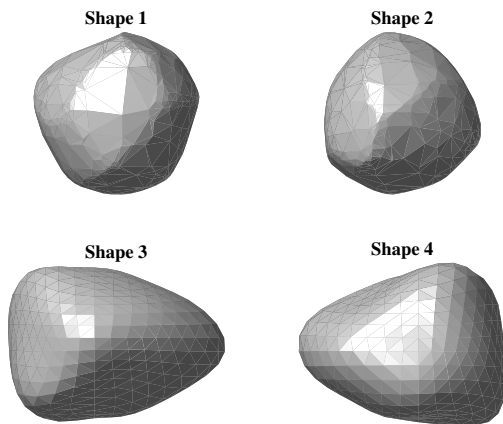


Figure 10. The four shape models of (24) Themis from the Database of Asteroid Models from Inversion Techniques. The shape models are shown in the same on-sky orientation.

12 (W2), and 22 (W2) μm with resolutions from 6.1'' to 12''. All four bands were imaged simultaneously, and the exposure times were 7.7 s in 3.4 and 4.6 μm and 8.8 s in 12 and 22 μm . The four-bands survey started from 2010 January 7, and ended on 2010 August 6 after the outer cryogen tank was exhausted, making the W4 channel be no longer able to be used to obtain survey data. The W3 channel continued operation until 2010 September 29 when the inner cryogen reserve was exhausted, while the W1 and W2 channel kept working until the telescope was set into hibernation on 2011 February 1. The two-band survey was then resumed on 2013 December 13 (known as NEOWISE), and is still in service, which has obtained nearly 6-year observations.

We found multi-year observations of Themis from WISE archive (see the website of the NASA/IPAC Infrared Science Archive <http://irsa.ipac.caltech.edu/>). The magnitude data are converted to flux with colour corrections (W1: 2.0577; W2: 1.3448; W3: 1.0006; W4: 0.9833), and all the derived monochromatic flux densities are set with an associated uncertainty of ± 10 percent (Wright et al. 2010). The flux data are summarized in Table 4, 5 and 6.

5.2. Input parameters

In order to interpret these multi-year observations, RSTPM needs several input parameters, including observation geometry, shape model, spin orientation, rotation phase ph , scattering weight-factor w_f , geometric albedo p_v , roughness fraction f_r , and mean grain radius \bar{b} .

The observation geometry at the time of each observation can be easily obtained according to the orbit of Themis and WISE. Spin orientation together with shape model has four different choices as listed in Table 3, which makes the rotation phase of each observation unclear as well. Hence the spin orientation would be the first parameter that need to be investigated by the fitting procedure.

The scattering weight-factor w_f is crucial in fitting procedure, as the W1 and W2 band observations contain significant amount of sunlight reflection. Since this parameter is an artificial factor used to interpret sunlight reflection, its physical significance isn't that clear, thus we only need a scattering weight-factor w_f that could achieve best-fitting degree to the observations.

The other parameters including geometric albedo p_v , roughness fraction f_r , and mean grain radius \bar{b} , are all free parameters that would be determined by optimization of fitting process.

5.3. Fitting with rotationally averaged flux: seasonal effect

As mentioned above, rotation phases at different observation epochs are unclear due to the uncertainties of spin orientation, thus at the first step, we choose the rotationally averaged model flux F_{model} to fit the observations, by which the diurnal effect is eliminated, whereas the seasonal effect is highlighted to investigate the influence of spin orientation.

5.3.1. Best-fit spin orientation

The available WISE/NEOWISE observations of Themis cover nearly 8 different epochs, as shown in Figure 11. Therefore, these observations of infrared flux can show seasonal variation, making it possible for us to investigate the probable spin orientation, roughness fraction and thermal parameters.

By fitting observations with rotationally averaged model flux generated by RSTPM under input of different spin orientation and physical parameters, best-fit results are selected out and summarized in Table 7.

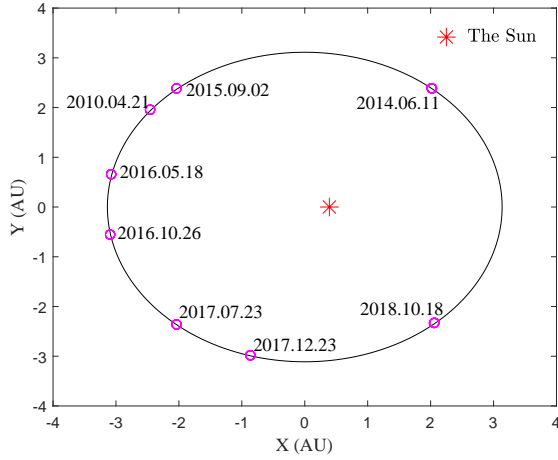
According to Table 7, in the case of shape 2, minimum reduced χ_r^2 is much smaller than that obtained in other three cases, indicating that shape 2 with spin orientation ($\lambda = 137^\circ$, $\beta = 59^\circ$) should be the best solution to the spin orientation and shape model of Themis. This result is consistent with the recent work of O'Rourke et al. (2020), which also concluded ($\lambda = 137^\circ$, $\beta = 59^\circ$) to be the best-fit spin orientation by TPM fitting to the Subaru/COMICS observations of Themis, indicating that this best solution of spin orientation is not accidental.

On the other hand, for the case of shape 2, we obtain best-fit scattering weight-factor $w_f = 0.32$. Then, in the following

Table 4. Mid-infrared observations of (24) Themis: WISE. The epoch marked by red is used as reference epoch to generate thermal light curves.

UT	Flux				MA (°)	r_{helio} (AU)	Δ_{obs} (AU)	α (°)
	$3.4 \mu\text{m}$ (mJy)	$4.6 \mu\text{m}$ (mJy)	$12 \mu\text{m}$ (Jy)	$22 \mu\text{m}$ (Jy)				
2010-04-21 00:45	3.59 ± 0.36	9.81 ± 0.98	4.95 ± 0.49	13.22 ± 1.32	131.584	3.421	3.278	17.082
2010-04-21 13:27	3.98 ± 0.40	10.50 ± 1.05	5.02 ± 0.50	15.05 ± 1.51	131.673	3.421	3.272	17.083
2010-04-21 15:02	3.65 ± 0.36	10.95 ± 1.10	6.20 ± 0.62	15.99 ± 1.60	131.687	3.421	3.270	17.083
2010-04-21 16:37	3.56 ± 0.36	10.57 ± 1.06	6.05 ± 0.61	16.28 ± 1.63	131.702	3.421	3.269	17.083
2010-04-21 18:13	3.67 ± 0.37	10.45 ± 1.05	5.29 ± 0.53	15.62 ± 1.56	131.710	3.421	3.269	17.083
2010-04-21 19:48	3.69 ± 0.37	11.13 ± 1.11	6.25 ± 0.62	17.08 ± 1.71	131.724	3.421	3.268	17.083
2010-04-21 21:23	3.66 ± 0.37	10.25 ± 1.03	5.73 ± 0.57	15.50 ± 1.55	131.732	3.421	3.267	17.083
2010-04-22 00:34	3.92 ± 0.39	10.81 ± 1.08	5.99 ± 0.60	16.03 ± 1.60	131.761	3.421	3.265	17.083
2010-04-22 03:44	3.98 ± 0.40	12.70 ± 1.27	6.30 ± 0.63	17.28 ± 1.73	131.783	3.422	3.263	17.083

MA: Orbital Mean Anomaly; α : solar phase angle.

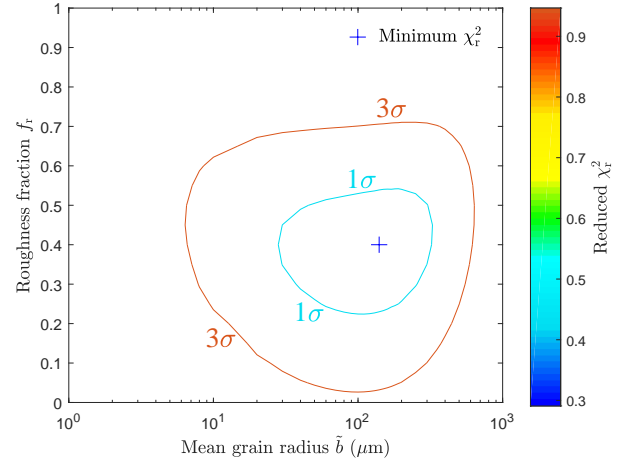
**Figure 11.** The little magenta circles represent orbital positions of (24) Themis at the time of each observation, covering 8 different epochs, making it possible to resolve the spin orientation, roughness fraction and thermal parameters by considering the seasonal variation of observed infrared flux by WISE/NEOWISE.

sections, we will utilize shape 2 and $w_f = 0.32$ to further study the geometric albedo p_v , roughness fraction f_r , mean grain radius \tilde{b} and thermal inertia Γ of Themis.

5.3.2. Results of p_v, f_r, \tilde{b}

By fixing shape model with spin orientation ($\lambda = 137^\circ$, $\beta = 59^\circ$) and scattering weight-factor $w_f = 0.32$, we then fit the observations by scanning roughness fraction f_r in the range of $0 \sim 1$ and mean grain radius \tilde{b} in the range of $1 \sim 1000 \mu\text{m}$. With each pair of (f_r, \tilde{b}) , a best-fit geometric albedo p_v together with effective diameter D_{eff} is found to compute the reduced χ_r^2 . The results are presented in Figure 12 as a contour of $\chi_r^2(f_r, \tilde{b})$.

According to Figure 12, a well constrained 1σ -level limit is derived for roughness fraction f_r and mean grain radius \tilde{b} , giving $f_r = 0.4 \pm 0.15$ (corresponding to RMS slope 31 ± 6), $\tilde{b} = 140^{+180}_{-110} \mu\text{m}$ respectively. 3σ -level constraint for roughness fraction is derived as $f_r = 0.4^{+0.3}_{-0.4}$ (corresponding to RMS slope 31^{+11}_{-31}), whereas for mean grain radius, a rela-

**Figure 12.** The contour of $\chi_r^2(f_r, \tilde{b})$, which is obtained by fitting the observations with two free parameters: roughness fraction f_r and mean grain radius \tilde{b} . The cyan region stands for the 1σ -level constraint, and the red region represents the 3σ -level constraint.

tively wide 3σ -level limit is obtained as $\tilde{b} = 140^{+500}_{-114} (6 \sim 640) \mu\text{m}$.

According to the above derived 1σ and 3σ ranges of roughness fraction and mean grain radius, the corresponding geometric albedo p_v and χ_r^2 are picked out, leading to the $p_v \sim \chi_r^2$ relation as shown in Figure 13. In this way, we obtain the 1σ and 3σ -level limits of geometric albedo as $p_v = 0.064^{+0.004}_{-0.005}$ and $p_v = 0.064^{+0.008}_{-0.011}$ respectively, and consequently the effective diameter of Themis can be derived to be $D_{\text{eff}} = 201.6^{+8.4}_{-5.9} \text{ km}$ (1σ) and $D_{\text{eff}} = 201.6^{+19.9}_{-11.5} \text{ km}$ (3σ) in consideration of the absolute visual magnitude $H_v = 7.08$ and slope parameter $G = 0.19$ (Harris et al. 1989).

Our result of geometric albedo $p_v = 0.064^{+0.008}_{-0.011}$ of Themis agrees with the result $p_v = 0.07 \pm 0.01$ of O'Rourke et al. (2020) in the range $0.06 \sim 0.072$, despite that our result tends to be smaller, which consequently leads to a larger estimation of effective diameter $D_{\text{eff}} = 201.6^{+19.9}_{-11.5} \text{ km}$ in comparison to the result $D_{\text{eff}} = 192^{+10}_{-7} \text{ km}$ derived by O'Rourke et al. (2020). Differences including data inputs and modeling procedures between our work and O'Rourke et al. (2020) may

Table 5. Mid-infrared observations of (24) Themis: NEOWISE (2014-2016).

UT	Flux (mJy)		MA (°)	r_{helio} (AU)	Δ_{obs} (AU)	α (°)
	3.4 μm	4.6 μm				
2014-06-10 20:42	7.65±0.76	38.43±3.84	39.354	2.854	2.633	-20.826
2014-06-10 20:43	7.80±0.78	40.10±4.01	39.354	2.854	2.633	-20.826
2014-06-10 23:52	7.48±0.75	36.84±3.68	39.376	2.854	2.635	-20.826
2014-06-11 03:01	7.47±0.75	36.10±3.61	39.398	2.854	2.636	-20.827
2014-06-11 06:11	7.54±0.75	41.18±4.12	39.421	2.854	2.638	-20.828
2014-06-11 07:46	7.25±0.73	34.22±3.42	39.435	2.854	2.639	-20.828
2014-06-11 09:20	7.21±0.72	36.07±3.61	39.443	2.854	2.640	-20.829
2014-06-11 10:55	7.39±0.74	35.15±3.51	39.458	2.854	2.641	-20.828
2014-06-11 12:30	7.60±0.76	37.15±3.71	39.472	2.855	2.642	-20.828
2014-06-11 14:05	7.48±0.75	41.30±4.13	39.480	2.855	2.643	-20.829
2014-06-11 15:39	7.25±0.73	35.08±3.51	39.495	2.855	2.644	-20.828
2014-06-11 17:14	7.53±0.75	37.28±3.73	39.502	2.855	2.644	-20.829
2014-06-11 20:24	7.21±0.72	35.08±3.51	39.524	2.855	2.646	-20.830
2014-06-11 23:33	7.63±0.76	37.28±3.73	39.554	2.855	2.649	-20.829
2014-06-12 02:43	7.48±0.75	36.07±3.61	39.576	2.855	2.650	-20.829
2015-08-31 14:31	4.48±0.45	12.51±1.25	118.614	3.360	3.066	-17.304
2015-09-01 01:32	4.83±0.48	11.53±1.15	118.695	3.360	3.072	-17.316
2015-09-01 03:07	4.23±0.42	11.02±1.10	118.702	3.360	3.073	-17.318
2015-09-01 06:16	4.05±0.40	11.05±1.11	118.725	3.360	3.075	-17.321
2015-09-01 06:16	4.05±0.40	11.05±1.11	118.725	3.360	3.075	-17.321
2015-09-01 07:50	3.21±0.32	11.34±1.13	118.739	3.361	3.076	-17.323
2015-09-01 10:59	4.18±0.42	10.98±1.10	118.762	3.361	3.078	-17.326
2015-09-01 14:08	4.89±0.49	11.17±1.12	118.784	3.361	3.080	-17.329
2015-09-01 17:17	4.05±0.40	9.67±0.97	118.806	3.361	3.082	-17.332
2015-09-01 17:17	4.05±0.40	9.67±0.97	118.806	3.361	3.082	-17.332
2016-05-17 11:02	3.24±0.32	7.95±0.79	164.647	3.519	3.384	16.700
2016-05-17 14:10	3.45±0.34	8.73±0.87	164.669	3.519	3.383	16.701
2016-05-17 17:19	3.39±0.34	7.93±0.79	164.691	3.519	3.381	16.701
2016-05-17 17:19	3.39±0.34	7.93±0.79	164.691	3.519	3.381	16.701
2016-05-17 18:53	3.26±0.33	8.01±0.80	164.706	3.519	3.380	16.702
2016-05-17 20:28	3.22±0.32	7.62±0.76	164.713	3.519	3.379	16.702
2016-05-17 22:02	3.34±0.33	8.42±0.84	164.728	3.519	3.378	16.702
2016-05-17 23:37	3.43±0.34	7.78±0.78	164.743	3.519	3.377	16.703
2016-05-18 01:11	3.31±0.33	7.66±0.77	164.750	3.519	3.376	16.702
2016-05-18 04:19	3.18±0.32	8.02±0.80	164.772	3.519	3.374	16.703
2016-05-18 07:28	3.47±0.35	8.65±0.86	164.794	3.520	3.373	16.703
2016-10-26 01:06	3.87±0.39	8.87±0.89	-166.726	3.522	3.137	-15.848
2016-10-26 04:15	4.00±0.40	9.37±0.94	-166.704	3.522	3.138	-15.856
2016-10-26 07:24	3.93±0.39	9.06±0.91	-166.682	3.522	3.140	-15.864
2016-10-26 08:58	3.57±0.36	8.51±0.85	-166.667	3.522	3.141	-15.869
2016-10-26 10:32	3.59±0.36	8.07±0.81	-166.653	3.522	3.143	-15.875
2016-10-26 12:07	3.98±0.40	10.18±1.02	-166.645	3.522	3.143	-15.877
2016-10-26 13:41	3.70±0.37	7.85±0.78	-166.630	3.522	3.144	-15.883
2016-10-26 15:15	4.11±0.41	8.78±0.88	-166.623	3.522	3.145	-15.885
2016-10-26 18:24	3.64±0.36	8.27±0.83	-166.601	3.522	3.147	-15.893
2016-10-27 00:41	3.75±0.38	8.76±0.88	-166.549	3.522	3.151	-15.911

MA: Orbital Mean Anomaly; α : solar phase angle.

both contribute to the slight differences of geometric albedo and effective diameter.

To verify the reliability of outcomes derived by the above fitting procedure, we employ the ratio of observation/model to examine how the model results match the observations at various observation wavelengths and geometries (Figure 14), because these factors are the basic variables of the observations.

The upper panel of Figure 14 show the observation/model ratios at each observation wavelength, where the ratios are evenly distributed around 1.0 without significant wavelength dependent features, indicating that the surface emissivity or

Table 6. Mid-infrared observations of (24) Themis: NEOWISE (2017-2018).

UT	Flux (mJy)		MA (°)	r_{helio} (AU)	Δ_{obs} (AU)	α (°)
	3.4 μm	4.6 μm				
2017-07-23 04:59	3.78±0.38	10.48±1.05	-118.84	3.361	3.199	17.596
2017-07-23 08:07	3.70±0.37	10.44±1.04	-118.82	3.360	3.197	17.596
2017-07-23 11:16	3.84±0.38	11.18±1.12	-118.79	3.360	3.195	17.596
2017-07-23 14:24	3.99±0.40	11.52±1.15	-118.77	3.360	3.194	17.597
2017-07-23 17:33	3.79±0.38	10.50±1.05	-118.74	3.360	3.191	17.597
2017-07-23 19:07	3.78±0.38	11.04±1.10	-118.74	3.360	3.190	17.597
2017-07-23 20:41	3.93±0.39	10.80±1.08	-118.72	3.360	3.189	17.597
2017-07-23 22:15	3.76±0.38	10.83±1.08	-118.72	3.360	3.188	17.597
2017-07-24 01:24	3.74±0.37	10.08±1.01	-118.69	3.360	3.187	17.597
2017-07-24 04:33	3.79±0.38	10.69±1.07	-118.66	3.360	3.184	17.597
2017-07-24 07:41	4.06±0.41	12.58±1.26	-118.64	3.360	3.182	17.597
2017-07-24 10:50	4.08±0.41	11.20±1.12	-118.62	3.359	3.180	17.596
2017-12-22 12:18	5.93±0.59	17.34±1.73	-91.832	3.198	2.731	-16.854
2017-12-22 15:27	6.02±0.60	18.06±1.81	-91.809	3.197	2.733	-16.867
2017-12-22 18:35	6.36±0.64	21.22±2.12	-91.780	3.197	2.735	-16.885
2017-12-22 20:10	5.80±0.58	16.43±1.64	-91.772	3.197	2.735	-16.890
2017-12-22 21:44	6.03±0.60	18.28±1.83	-91.758	3.197	2.736	-16.899
2017-12-22 23:18	6.01±0.60	18.29±1.83	-91.750	3.197	2.737	-16.903
2017-12-23 00:52	5.80±0.58	17.06±1.71	-91.735	3.197	2.738	-16.912
2017-12-23 00:53	5.75±0.58	17.57±1.76	-91.735	3.197	2.738	-16.912
2017-12-23 02:27	6.15±0.62	20.72±2.07	-91.728	3.197	2.739	-16.916
2017-12-23 02:27	6.15±0.62	20.72±2.07	-91.728	3.197	2.739	-16.916
2017-12-23 05:35	6.16±0.62	18.08±1.81	-91.698	3.197	2.741	-16.934
2017-12-23 08:44	5.77±0.58	17.50±1.75	-91.676	3.196	2.742	-16.947
2017-12-23 11:52	5.93±0.59	19.16±1.92	-91.654	3.196	2.744	-16.960
2018-10-17 10:08	7.00±0.70	39.33±3.93	-38.793	2.854	2.685	20.440
2018-10-17 13:17	7.17±0.72	41.76±4.18	-38.770	2.853	2.684	20.441
2018-10-17 16:25	7.42±0.74	39.55±3.95	-38.748	2.853	2.682	20.441
2018-10-17 19:34	8.19±0.82	42.65±4.27	-38.719	2.853	2.680	20.441
2018-10-17 19:34	8.19±0.82	42.65±4.27	-38.719	2.853	2.680	20.441
2018-10-17 22:42	7.28±0.73	38.26±3.83	-38.697	2.853	2.678	20.441
2018-10-18 00:16	7.20±0.72	40.73±4.07	-38.689	2.853	2.677	20.442
2018-10-18 01:51	7.43±0.74	40.02±4.00	-38.674	2.853	2.676	20.441
2018-10-18 03:24	7.44±0.74	40.99±4.10	-38.667	2.853	2.675	20.442
2018-10-18 04:58	7.48±0.75	46.38±4.64	-38.652	2.853	2.674	20.442
2018-10-18 06:33	7.29±0.73	40.06±4.01	-38.637	2.853	2.673	20.442
2018-10-18 09:42	7.38±0.74	39.37±3.94	-38.615	2.853	2.671	20.442
2018-10-18 12:50	8.44±0.84	44.46±4.45	-38.593	2.853	2.669	20.442
2018-10-18 15:58	7.66±0.77	41.68±4.17	-38.571	2.852	2.667	20.442

MA: Orbital Mean Anomaly; α : solar phase angle.

Table 7. Best-fit results by fitting observations with rotationally averaged model flux.

	Best-fitting parameters				Minimum χ^2_r
	w_f	p_v	f_r	\bar{b} (μm)	
shape 1	0.37	0.067	0.45	150	0.383
shape 2	0.32	0.064	0.40	140	0.291
shape 3	0.50	0.058	0.50	140	0.982
shape 4	0.50	0.060	0.50	140	0.842

w_f : scattering weight-factor.

f_r : roughness fraction; \bar{b} : mean grain radius.

albedo of Themis do not show significant wavelength dependence, thus the combination model of surface thermal emission and sunlight reflection is good enough to interpret WISE/NEOWISE observations of Themis.

The lower panel of Figure 14 presents the observation/model ratios at different solar phase angles, where the ratios are also uniformly distributed round 1.0, showing no

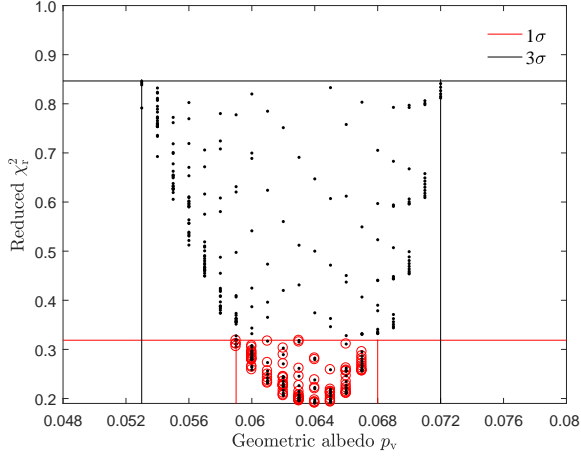


Figure 13. $p_v \sim \chi_{\text{reduced}}^2$ profiles fit to the observations in consideration of the derived 1σ and 3σ ranges of roughness fraction and mean grain radius.

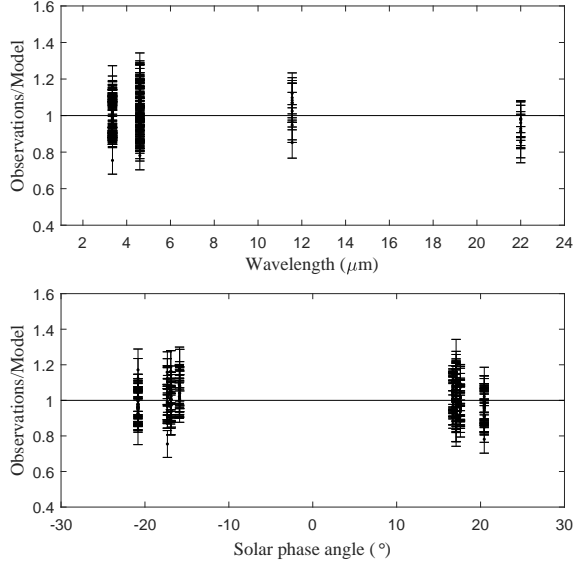


Figure 14. The observation/model ratios as a function of wavelength (upper panel) and solar phase angle (under panel) for the case of best-fit parameters.

distinct phase-angle dependent features, indicating that the thermal infrared beaming effect of Themis is well resolved by our model, and hence the expectation of removing the degeneracy between thermal parameters and roughness by multi-epoch data is well realised. Therefore, it should be safe to claim that the above fitting procedure and derived results are reliable.

5.3.3. Seasonal variation of thermal inertia

As illustrated in section 3.3, thermal inertia is a strong function of temperature. Now with the above derived profile of mean grain radius, we can evaluate the change of surface

thermal inertia of Themis due to the influence of seasonal temperature variation.

In Figure 15, a map of surface temperature of Themis is plotted as a function of local latitude and orbital mean anomaly. Each temperature has been averaged over one rotational period. We can clearly see that temperature on each local latitude can reach maximum (summer) or minimum (winter) at different orbital positions as a result of seasonal effect. Temperature on the poles can vary from ~ 34 K to ~ 206 K.

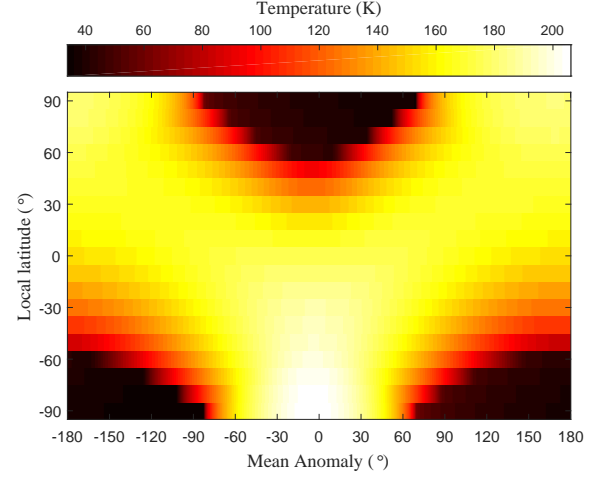


Figure 15. Seasonal variation of the diurnal-averaged surface temperature as a function of local latitude. The so-called local latitude is defined as the complementary angle of the angle between the local normal vector and the rotation axis.

The significant temperature variation caused by seasonal effect can have influence on the thermal inertia of surface materials. With Equation (59), (58) and (57), variation of surface thermal inertia can be evaluated, as shown in Figure 16. If considering 3σ -level results of mean grain radius \bar{b} , surface thermal inertia of Themis may vary from a minimum profile of $\sim 3 \text{ Jm}^{-2}\text{s}^{-0.5}\text{K}^{-1}$ to a maximum value of $\sim 60 \text{ Jm}^{-2}\text{s}^{-0.5}\text{K}^{-1}$. Moreover, Figure 16 shows that, in comparison to the uncertainties of mean grain radius, influence of temperature variation on thermal inertia is more significant.

5.3.4. Average thermal inertia

Despite the fact that thermal inertia is temperature dependent, the majority of relevant works ignore such temperature dependence and only estimate the average thermal inertias. For comparison with such existing results, we estimate the seasonal average thermal inertia of Themis by using Equation (59), (58) and (57) with inputs of the derived mean grain radius and seasonal averaged temperature of Themis. The seasonal average temperature would be a function of local latitude, $\bar{T}(\theta)$, and can be estimated as

$$(1 - A_{\text{eff,B}})\bar{L}_s(\theta) = \varepsilon\sigma\bar{T}(\theta)^4, \quad (77)$$

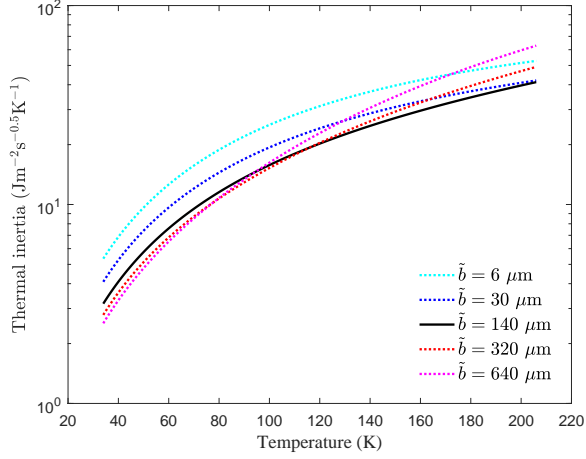


Figure 16. Change of surface thermal inertia of Themis due to seasonal temperature variation, considering 3σ -level uncertainties of mean grain radius \tilde{b} .

where $A_{\text{eff,B}}$ is the bond albedo, $\varepsilon \sim 0.9$ is the average thermal emissivity, $\tilde{L}_s(\theta)$ is the annual average incoming solar flux on each latitude. The results are presented in Figure 17.

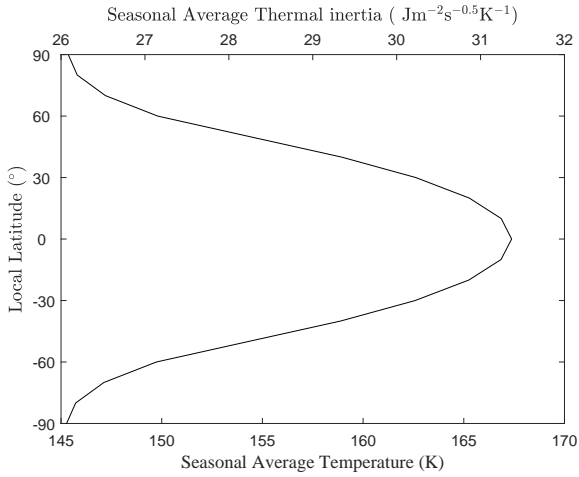


Figure 17. Seasonal average temperature and thermal inertia of (24) Themis.

From Figure 17, we see that the average thermal inertia of Themis would be within $26 \sim 32 \text{ Jm}^{-2}\text{s}^{-0.5}\text{K}^{-1}$. As a comparison, our result of average thermal inertia is well consistent with that of O'Rourke et al. (2020), which estimated Themis to have a mean thermal inertia of $\sim 20^{+25}_{-10} \text{ Jm}^{-2}\text{s}^{-0.5}\text{K}^{-1}$.

5.4. Fitting with thermal light curve: diurnal effect

Since the WISE/NEOWISE data at different epochs do not perfectly cover an entire rotation period and have been observed at various solar phase angles, it is not proper to directly use them to generate thermal light curves. However,

orbital and rotational parameters of Themis is well known. Thus, in principle, we could derive the rotational phase of each observation data with respect to a defined local body-fixed coordinate system if we know the observed rotational phase at a particular epoch. These data could then be used to create thermal light curves.

The 3D shape model is used to define the local body-fixed coordinate system, where the z-axis is chosen to be the rotation axis, and "zero" rotational phase is chosen to be the "Equatorial view (0°)" as shown in Figure 18. Moreover, if we define the view angle of one observation with respect to the body-fixed coordinate system to be (φ, θ) , where φ stands for local longitude, and θ means local latitude, then the rotational phase ph of this observation can be related to the local longitude φ via

$$ph = 1 - \varphi/(2\pi). \quad (78)$$

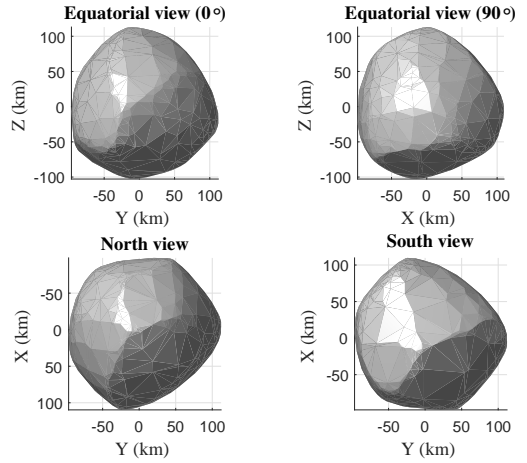


Figure 18. 3D shape model used to define the local body-fixed coordinate system, where the "zero" rotational phase is chosen to be the Equatorial view 0° (view along the x-axis, with the y-axis extending horizontally and the z-axis extending vertically).

If selecting a reference epoch, and assuming the rotational phase at this epoch to be zph , then all the rotational phases of other data could be derived in consideration of the observation time and geometry. Furthermore, for some particular epoch, thermal light curves can be derived for each band by correcting the observed flux at various epochs into one rotation period at this epoch, where the correction is implemented via

$$F_{i,\text{corr}} = F_i \left(\frac{r_{i,\text{helio}}}{r_{0,\text{helio}}} \right)^2 \left(\frac{\Delta_{i,\text{obs}}}{\Delta_{0,\text{obs}}} \right)^2, \quad (79)$$

in which $F_{i,\text{corr}}$ is the flux after correction, F_i is the original observed flux, $r_{i,\text{helio}}$ and $r_{0,\text{helio}}$ are the heliocentric distance of epoch i and the reference epoch, while $\Delta_{i,\text{obs}}$ and $\Delta_{0,\text{obs}}$ are the observation distance.

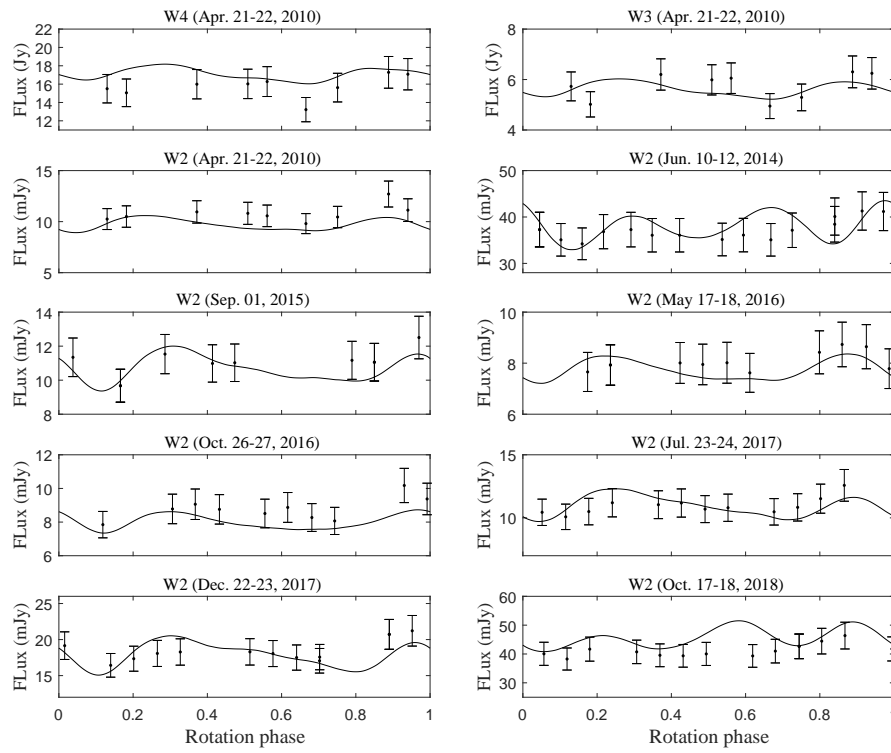


Figure 19. Best-fit results to the thermal light curves of WISE/NEOWISE at band W4, W3, W2.

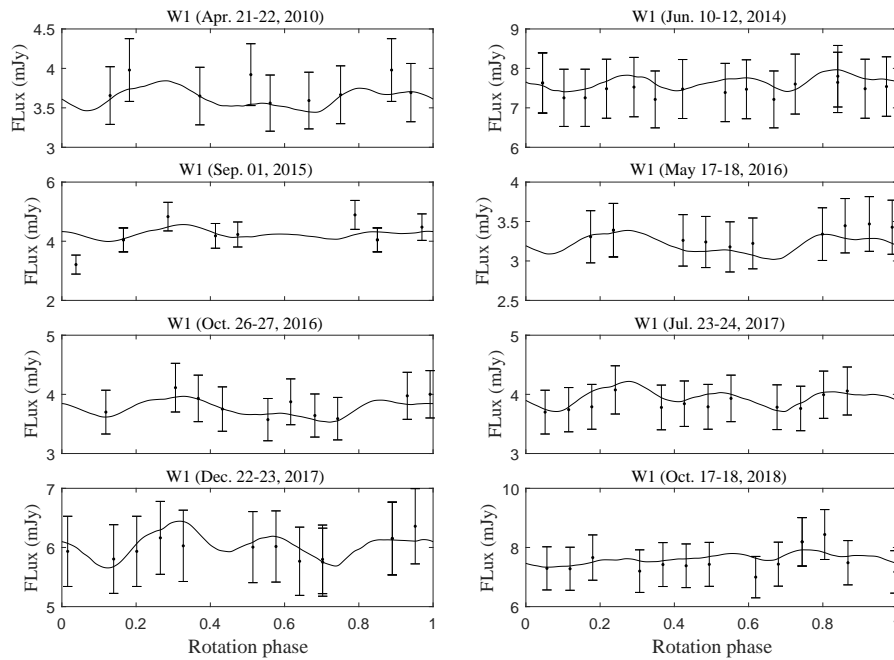


Figure 20. Best-fit results to the light curves of WISE/NEOWISE at band W1.

Following the above method, firstly we select '2014-06-10 20:42' as the reference epoch for deriving the reference rotational phase zph . But for correction of flux, in order to reduce flux errors caused by correction Equation (79), we select 8 separate reference epochs, so as to use data close to each reference epoch (data within three days) to generate thermal light curves. These 8 reference epochs are marked with red color in Table 4, 5 and 6. Then for each of the reference epoch, theoretical thermal light curves are simulated by RSTPM to fit the above generated observations of thermal light curves. The best-fit results are plotted in Figure 19 and 20.

Now questions arise what we can learn by fitting with thermal light curves. Since both irregular shape and surface heterogeneity can contribute to the rotational variation of flux in light-curves, so we can evaluate whether the surface has heterogeneity along longitude by fitting with thermal light curves. To realize this purpose, we can investigate whether the ratios of observation/model have rotation phase dependent features.

Note that the fraction of sunlight-reflection in each band observation of WISE/NEOWISE is significantly different. To show such differences, best-fit parameters are input to RSTPM to estimate the fraction of sunlight-reflection in each band observation at each epoch. The results are shown in in Figure 21, where we can see that the fraction of reflection is almost zero at bands W4 and W3 ($< 10^{-4}$), but comes to be non-negligible at band W2 ($\sim 10 - 30\%$), and becomes dominating at band W1 (reaches up to $\sim 99\%$), so the observation/model ratios for bands W4 and W3 actually represents the deviation of real thermal emissivity relative to the model-input emissivity ≈ 0.9 , while the ratios of observation/model for band W1 stand for deviation of real geometric albedo from the best-fit value ≈ 0.064 .

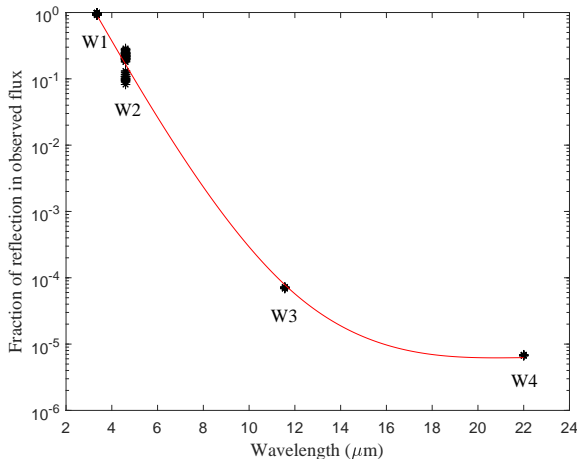


Figure 21. The fraction of sunlight-reflection in the observed flux of Themis for each band of WISE/NEOWISE.

Therefore, the ratios of observation/model for each band are separately plotted as a function of rotation phase in Fig-

ure 22. From Figure 22, we see that the observation/model ratios for band W1 are evenly distributed around 1.0 at all rotation phases, showing no rotation-phase dependent feature, hence indicating that the light-curve inversion shape model fits the W1-band data pretty good and surface albedo of Themis doesn't significantly vary with longitude. However, for band W4, W3 and W2, the observation/model ratios show a weak rotation-phase dependent feature, as shown by the red dashed-curves in Figure 22, where variation trend of the three red dashed-curves are similar to each other but different from the trend of W1, indicating that surface materials on different longitude of Themis may have heterogeneous thermal properties if the shape model imperfection is small. However, the light-curve inversion shape model is only an ideal shape that achieves optimum fitting to the visible lightcurves. It may be still different to the real shape, and hence may not be able to produce thermal light-curve very well. Therefore, the possibility of trends in W2, W3, and W4 thermal lightcurves being caused by shape model imperfections cannot be removed.

6. DISCUSSION AND CONCLUSION

Thermophysical modelling is the basis of thermal infrared radiometry, which is the main method to measure thermophysical properties of surface materials on small bodies. So developing advanced thermophysical models have been always the direction of work in this field. For airless small bodies, the thermal state of the surface layers is influenced not only by the surface thermophysical parameters, but also by geometric effect like roughness or topography, and kinestate including rotation and orbital motion. The complexity of the problem lies in that these effects' influence on the thermal state are coupled together, making that surface thermal parameters and roughness have inevitable degeneracy in the radiometry procedure, hence multi-epoch observations are necessary to remove the degeneracy of thermal inertia and roughness in the radiometric procedure. Therefore, for the use of interpreting multi-epoch thermal lightcurves (e.g WISE/NEOWISE), we propose this thermophysical model for realistic surface layers on airless small bodies — RSTPM, which simultaneously considers real orbital cycle, rotation cycle, rough surface, temperature dependent thermal parameters, as well as contributions of sunlight reflection to observation.

When we aim to interpret multi-epoch observations, the temperature dependence of thermal inertia becomes non-negligible if seasonal effect can cause significant temperature variation. As shown in Figure 16, seasonal temperature variation's influence on thermal inertia can be more significant than the influence from the uncertainties of mean dust-grain size, if there is a dust mantle on the surface, and thermal conductivity of the dust mantle can be related to the temperature, porosity of the dust mantle and mean dust-grain radius like Equation (58). Therefore, for such small bodies covered by dust mantle, the mean dust-grain size of dust mantle is more suitable to be used as the free parameter to be determined from the radiometric procedure, which then provides a way

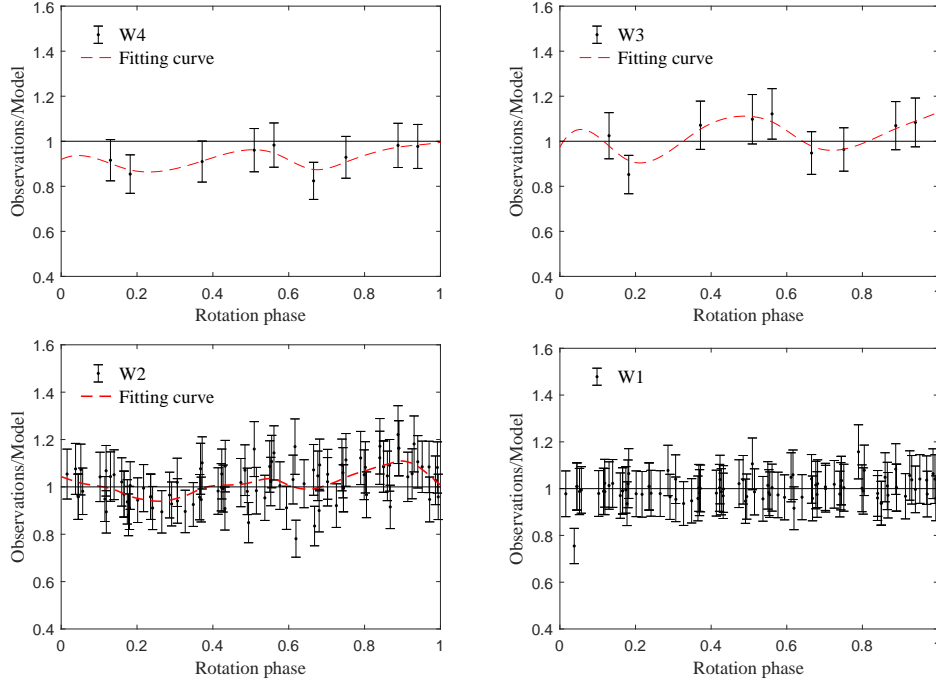


Figure 22. Ratios of observation/model as a function of rotation phase for each band respectively.

to study the physical properties of dust on the surface of small bodies.

Of course, there are also small bodies that don't have dust mantle on the surface. For example, in-situ observations of (162173) Ryugu by Hayabusa2 show that most of Ryugu's surface is covered by porous boulders (Okada et al. 2020). For such small bodies, there is even no dust mantle on the surface, hence there is no need to study dust properties, and thermal inertia can not be modelled as a function of mean dust grain size, whereas RSTPM can be still used to study the mean thermal inertia of the surface, or the macroscopic porosity of the surface if the thermal inertia can be described as a function of temperature and porosity.

Dust mantle is more likely to appear on large main belt objects, so WISE/NEOWISE becomes a versatile archive to study dust properties of these bodies. However, as shown in Figure 21, the W1-band observation is actually dominated by sunlight-reflection, and even the W2-band observation contains non-negligible $\sim 10 - 30\%$ sunlight-reflection. Thus, a precise combination model of thermal emission and sunlight reflection is extremely necessary to interpret multi-epoch thermal light-curves of WISE/NEOWISE. RSTPM perform very well in simultaneously simulating the thermal emission and sunlight reflection, as demonstrated by its successful application to (24) Themis. But it should be noted that the

"scattering weight-factor" w_f used in the reflection model (Equation 64) is an artificial factor, which doesn't have clear physical significance, and may need further examination by more observations and researches.

Nevertheless, the successful application of RSTPM makes it possible for us to claim that this model is reliable, and is highly capable to derive the physical properties of small bodies by interpreting the four-band WISE/NEOWISE observations obtained at multiple epochs. We thus propose: if used to fit rotationally averaged observations of multiple epochs, RSTPM can study the spin orientation as well as surface properties, including geometric albedo, roughness and mean thermal inertia or mean dust-grain size; if used to fit thermal light curves, RSTPM can investigate whether surface materials on different longitude are heterogeneous in terms of thermophysical properties.

ACKNOWLEDGMENTS

We thank the NASA-WISE teams for providing public data. This work was supported by the grants from The Science and Technology Development Fund, Macau SAR (No. 119/2017/A2, 061/2017/A2 and 0007/2019/A) and Faculty Research Grants of The Macau University of Science and Technology (program no. FRG-19-004-SSI).

REFERENCES

- Bowell, E., Hapke, B., Domingue, D., et al., 1989. Application of photometric models to asteroids. In *Asteroids II*, pp. 524-556
- Britt, D. T., Yeomans, D., Housen, K., & Consolmagno, G., 2002. Asteroid Density, Porosity, and Structure. In *Asteroids III* (Eds. Bottke Jr., W. F., Cellino, A., Paolicchi, P., and Binzel, R. P.), Univ. Arizona Press, Tucson, pp.485-500

- Davidsson, B. J. R., & Rickman, H., 2014, *Icarus*, 243, 58-77
- Delbo, M., 2004. The nature of near-Earth asteroids from the study of their thermal infrared emission. PhD thesis
- Delbo, M., Mueller, M., Emery, J., Rozitis, B., & Capria, M. T., 2015. Asteroid Thermophysical Modeling. In *Asteroids IV* (Eds. by Michel, P., DeMeo, F.E., Bottke, W.F.), Univ. Arizona Press, Tucson, pp. 107-128
- Fowler, J. W., & Chillemi, J. R., 1992. IRAS asteroids data processing, In *The IRAS Minor Planet Survey*, pp. 17-43
- Gundlach, B., Blum, J., 2013, *Icarus*, 223, 479-492
- Hanuš, J., Delbo, M., Ďurech, J., & Ali-Lagoa, V., 2015, *Icarus* 256, 101-116
- Hanuš, J., Ďurech, J., Oszkiewicz, D. A., et al., 2016, *A&A*, 586, A108
- Harris, A. W., Yong, J. W., Bowell, E., et al., 1989, *Icarus* 77, 171-186
- Kaasalainen, M., & Torppa J., 2001, *Icarus*, 153, 24
- Kaasalainen, M., Torppa, J., & Muinonen, K., 2001, 153, 37
- Lagerros, J. S. V., 1996, *A&A*, 310, 1011-1020.
- Lagerros, J. S. V., 1996, *A&A*, 315, 625-632.
- Lagerros, J. S. V., 1997, *A&A*, 325, 1226-1236.
- Lagerros, J. S. V., 1998, *A&A*, 332, 1123-1132.
- Macke, R. J., Opeil, C. P., Consolmagno, G. J. and Britt, D. T., 2016. Ordinary Chondrite heat capacities below 350K, 47th Lunar and Planetary Science Conference, LPI Contribution No. 1903, p.1221
- Mainzer A. et al., 2011, *ApJ*, 731, 53
- Okada, T., Fukuhara, T., Tanaka, S., et al., 2020, *Nature*, 579, 518-522
- Opeil, C. P., Consolmagno, G. J., Britt, D. T., 2010, *Icarus*, 208, 449-454
- Opeil, C. P., & Britt, D. T., 2016. Thermal Expansion, Heat Capacity and Thermal Conductivity Measurements of CM Carbonaceous Chondrites, Asia Oceania Geosciences Society Conference, Beijing, China, Abstract No. PS11-A018
- O'Rourke, L., Müller, T. G., Biver, N., et al., 2020, *ApJL*, 898, L45
- Ostro, S.J., Hudson, R.S., Benner, L.A.M., et al., 2002. Asteroid radar astronomy. In *Asteroids III*, Univ. Arizona Press, Tucson, pp. 151-168
- Rozitis, B., & Green, S. F., 2011, *MNRAS*, 415, 2042
- Rozitis, B., & Green, S. F., MacLennan E., Emery J.P., 2018, *MNRAS*, 477, 1782
- Spencer, J. R., 1990. A Rough-Surface Thermophysical Model for Airless Planets, *Icarus*, 83, 27-38
- Viikinkoski, M., Hanuš, J., Kaasalainen, M., et al., 2017, *A&A*, 607, A117
- Waples, D.W., & Waples J.S., 2004, *Natural Resources Research*, 13, 2
- Wasson, J.T., & Kallemeyn, G.W., 1988. Composition of chondrites, *Philosophical Transactions of The Royal Society A*, 325, 538-544
- Wright, E. L., Eisenhardt, P. R. M., & Mainzer, A. K., et al. 2010, *AJ*, 140, 1868
- Yu, L.L., Yang, B., Ji, J.H., & Ip, W.H., 2017, *MNRAS*, 472, 2388-2397
- Yu L. L., Ip W. H., & Spohn T., 2019, *MNRAS*, 482, 4243